FATIGUE CRACK GROWTH BEHAVIOR OF HOT ROLLED AA2050-T84 PLATES

A THESIS SUBMITTED TO
THE GRADUATE SCHOOL OF NATURAL AND APPLIED SCIENCES
OF
MIDDLE EAST TECHNICAL UNIVERSITY

BY

BEGÜM ATA TUFAN

IN PARTIAL FULFILLMENT OF THE REQUIREMENTS
FOR
THE DEGREE OF MASTER OF SCIENCE
IN
METALLURGICAL AND MATERIALS ENGINEERING

SEPTEMBER 2023

Approval of the thesis:

FATIGUE CRACK GROWTH BEHAVIOR OF HOT ROLLED AA2050-T84 PLATES

submitted by **BEGÜM ATA TUFAN** in partial fulfillment of the requirements for the degree of **Master of Science** i**n Metallurgical and Materials Engineering, Middle East Technical University** by,

Prof. Dr. Halil Kalıpçılar
Dean, Graduate School of **Natural and Applied Sciences** _____

Prof. Dr. Ali Kalkanlı
Head of the Department, **Metallurgical and Materials Engineering** _____

Prof. Dr. Rıza Gürbüz
Supervisor, **Metallurgical and Materials Engineering, METU** _____

Examining Committee Members:

Prof. Dr. Bilgehan Ögel
Metallurgical and Materials Eng, METU _____

Prof. Dr. Rıza Gürbüz
Metallurgical and Materials Eng, METU _____

Prof. Dr. Cevdet Kaynak
Metallurgical and Materials Eng, METU _____

Prof. Dr. C. Hakan Gür
Metallurgical and Materials Eng., METU _____

Prof. Dr. Benat Koçkar
Mechanical Engineering, Hacettepe Üniversitesi _____

Date: 11.09.2023

I hereby declare that all information in this document has been obtained and presented in accordance with academic rules and ethical conduct. I also declare that, as required by these rules and conduct, I have fully cited and referenced all material and results that are not original to this work.

Name Last name : Begüm Ata Tufan

Signature :

ABSTRACT

FATIGUE CRACK GROWTH BEHAVIOR OF HOT ROLLED AA2050-T84 PLATES

Ata Tufan, Begüm
Master of Science, Metallurgical and Materials Engineering
Supervisor: Prof. Dr. Rıza Gürbüz

September 2023, 83 pages

Lithium-containing aluminum alloys have gained prominence in aerospace applications due to their lower density and improved elastic modulus compared to other aluminum alloys. Aluminum-lithium alloys have been developed to address weight and performance requirements in future aircraft. Among the third-generation aluminum-lithium alloys, AA2050 has emerged as a potential replacement for incumbent plate alloys, such as 7xxx and 2xxx alloys, offering high strength, fatigue crack growth resistance, and damage tolerance while enabling weight savings.

This study focuses on comprehensively characterizing the microstructure and mechanical properties of AA2050-T84 alloy. Two hot rolled plates having 20 mm and 130 mm thickness were used in this study. The plates underwent identical production stages except for the extent of hot rolling, which was higher for the 20 mm thick plate. A comparative analysis between the two plates aims to understand how the grain anisotropy and orientation affect the overall mechanical performance of the alloy. Moreover, fatigue tests and fatigue crack growth tests are conducted to assess the resistance of the alloy to cyclic loading-induced damage. Importantly, the highly anisotropic grain structure and the preferred crystallographic orientation in the 20 mm thick plate were found to cause a fatigue crack deviation. Fractographic analyses of the 20 mm thick plate (when the loading was parallel to the rolling direction) exhibited microcrack formations perpendicular to the crack growth

direction and slip bands at the intermediate ΔK. Collectively, the findings from this study contribute to the existing knowledge of AA2050 alloy properties and offer critical insights into how the rolling operation for achieving thin plates influences the microstructure and overall performance of the alloy.

Keywords: AA2050-T84, Fatigue Crack Growth, Fracture, Crack Deviation, Microstructure

ÖZ

SICAK HADDELENMİŞ AA2050-T84 PLAKALARIN YORULMA ÇATLAK İLERLEME DAVRANIŞI

Ata Tufan, Begüm
Yüksek Lisans, Metalurji ve Malzeme Mühendisliği
Tez Yöneticisi: Prof. Dr. Rıza Gürbüz

Eylül 2023, 83 sayfa

Lityum içeren alüminyum alaşımları, diğer alüminyum alaşımlarına kıyasla daha düşük yoğunluğa ve geliştirilmiş elastik modüle sahip olmaları nedeniyle havacılık uygulamalarında önem kazanmıştır. Havacılık sektöründe ağırlık ve performans gereksinimlerini karşılamak için alüminyum-lityum alaşımları geliştirilmiştir. Üçüncü nesil alüminyum-lityum alaşımları arasında, AA2050, yüksek dayanıklılık, yorulma çatlağı büyüme direnci ve hasar tolere edebilme özellikleriyle birlikte ağırlık tasarrufu sağlayarak, mevcut plaka alaşımları olan 7xxx ve 2xxx alaşımları için potansiyel bir alternatif olarak ortaya çıkmıştır.

Bu çalışma, AA2050-T84 alaşımının mikroyapısını ve mekanik özelliklerini kapsamlı bir şekilde karakterize etmeye odaklanmaktadır. Çalışmada 20 mm ve 130 mm kalınlıklara sahip sıcak haddeleme yöntemiyle üretilmiş plakalar kullanılmıştır. Plakalar haddeleme miktarı hariç (20 mm plaka için daha fazla miktarda haddeleme yapılmıştır) aynı üretim aşamalarından geçmiştir. İki farklı plaka seçilmesindeki temel amaç tane yönelimi ve anistropisinin alaşımın mekanik performansı üzerindeki etkisini araştırmaktır. Ayrıca, yorulma testleri ve yorulma çatlağı büyüme testleri, alaşımın döngüsel yükleme kaynaklı hasara karşı direncini değerlendirmek için gerçekleştirilmiştir. Özellikle, 20 mm kalınlığındaki plakanın hadde yönü yüklenme doğrultusuna paralel olduğu durumda, yüksek derecede anizotropik tane yapısı ve tercih edilen kristalografik yönelim yorulma çatlağı sapmasına neden olmuştur. 20

mm kalınlığındaki plakanın kırılma yüzeyi analizleri, çatlağın büyüme yönüne dik mikroçatlak oluşumunu ve orta seviyedeki ΔK'da kayma bantlarının meydana geldiğini göstermiştir. Bu çalışmadan elde edilen bulgular, AA2050 alaşımının malzeme özellikleri hakkındaki mevcut bilgiye katkıda bulunmakta ve ince plakaların elde edilmesinde uygulanan haddeleme işleminin alaşımın mikroyapısı ve genel performansı üzerindeki etkileri konusunda literature katkı yapacağı öngörülmektedir.

Anahtar Kelimeler: AA2050-T84, Yorulma Çatlak İlerlemesi, Kırılma, Çatlak Sapması, Mikroyapı

To my true love and my beloved family

ACKNOWLEDGMENTS

First and foremost, I express my gratitude to my supervisor, Prof. Dr. Rıza Gürbüz, who guided me throughout my studies with his comments, support, and friendly approach.

I extend my special thanks to Turkish Aerospace Industries for enabling the procurement of the samples used in this study and facilitating the performance of tests and analyses within the company facilities.

I wish to express my gratitude to Alp Aykut Kibar for his valuable advice, comments, and generous support. Special thanks to Müfit Kacar, Münevver Eryılmaz, and Kadir Karaman for their assistance in the mechanical tests and friendly support. I am also deeply grateful to Merve Yeşim Yalçın for her invaluable assistance in the EBSD analysis. I would like to thank Zeynep Özen for her assistance and pleasant companionship in preparing metallographic samples. I am thankful to my team colleagues Mustafa Anıl Yıldırım and Betül Kaya for their friendship and support.

Special thanks to Meryem Çiftçi, Özge Uludağ, and Yağmur Akbulut Atılgan for their unconditional friendship. I am profoundly thankful to my beloved parents, brother, mother-in-law, and father-in-law for the love and dedication they have demonstrated throughout this period. Finally, I am deeply thankful to my beloved husband, Yiğithan Tufan, for his invaluable comments and unwavering love and support throughout my thesis journey.

TABLE OF CONTENTS

LIST OF TABLES

TABLES

LIST OF FIGURES

FIGURES

LIST OF ABBREVIATIONS

ABBREVIATIONS

P20: 20 mm thick plate

P20_L-LT: L-LT plane of 20 mm thick plate

P20_L-ST: L-ST plane of 20 mm thick plate

P20_LT-ST: LT-ST plane of 20 mm thick plate

P20_L: L-oriented samples extracted from the 20 mm thick plate.

P20_LT: LT-oriented samples extracted from the 20 mm thick plate.

P20_L-T: CT specimen extracted from 20 mm thick plate, where L and T represents loading and crack growth directions, respectively.

P20_T-L: CT specimen extracted from 20 mm thick plate, where T and L represents loading and crack growth directions, respectively.

P130: 130 mm thick plate

P130_L-LT: L-LT plane of 130 mm thick plate

P130 _L-ST: L-ST plane of 130 mm thick plate

P130 _LT-ST: LT-ST plane of 130 mm thick plate

P130 _L: L-oriented samples extracted from the 130 mm thick plate.

P130 _LT: LT-oriented samples extracted from the 130 mm thick plate.

P130 _L-T: CT specimen extracted from 130 mm thick plate, where L and T represents loading and crack growth directions, respectively.

P130 _T-L: CT specimen extracted from 130 mm thick plate, where T and L represents loading and crack growth directions, respectively.

CHAPTER 1

INTRODUCTION

1.1 History of Aluminum-Lithium (Al-Li) Alloys

The production of the first commercial lithium-containing aluminum alloy, which originated in the 1920s, was discontinued due to the inconclusive findings regarding the strengthening effect of lithium [1,2]. Then, in 1945, it was discovered that lithium could be a major strengthening element in aluminum-copper alloys. This discovery paved the way for the development of modern aluminum-lithium alloys. In the 1950s, which could be considered another milestone for the development of lithium-containing aluminum alloys, lithium was found to increase the elastic modulus of aluminum, followed by the discovery of high-strength Al-Cu-Li alloy 2020 in 1957. The alloy consisted of approximately 4.5% copper and 1.2% lithium by weight [3]. It was commercially produced and used for over 20 years in manufacturing the wings of the United States Navy's RA-5C Vigilante aircraft successfully [4]. However, due to manufacturing challenges associated with its high brittleness and poor ductility, the 2020 alloy was eventually phased out from commercial applications. The decrease in the 2020 alloy's ductility can be attributed to the relatively high silicon (Si) and iron (Fe) content used. These elements tend to form insoluble phases during the solidification and subsequent processing of the alloy, which consequently leads to a reduction in its ductility [5]. Also, in the early 1960s, the Soviet Union developed alloys 01420 and 01421, which contained around 5.2% magnesium and 2.1% lithium by weight. Although these alloys offered the advantages of reduced density due to lithium and improved weldability resulting from adding magnesium, their strength and fracture toughness did not meet the requirements of modern aircraft [6]. The important stages of the development of lithium-containing aluminum alloys are chronologically listed in Figure 1.1 [7].

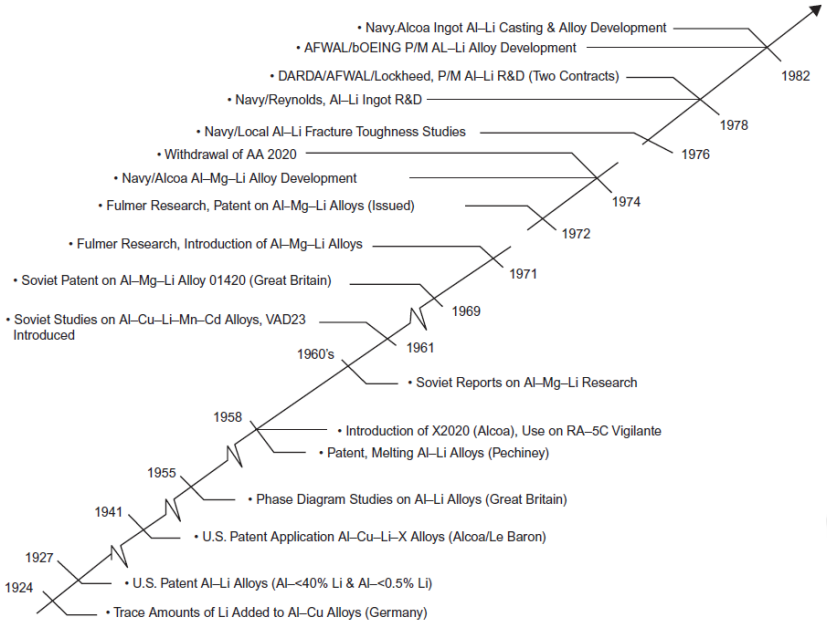

Figure 1.1. The chronological steps of the development of lithium-containing aluminum alloys [7].

Lithium-containing aluminum alloys are favored in aerospace applications as they possess a lower density and an improved elastic modulus compared to other aluminum alloys. For each wt% of lithium, the alloy density decreases by 3%, and the elastic modulus increases by 6% [8,9]. This decrease in density and increase in elastic modulus is the highest for lithium among all alloying elements (the effect of alloying elements on the density and Young's modulus of aluminum is shown in Figure 1.2a and Figure 1.2b, respectively).

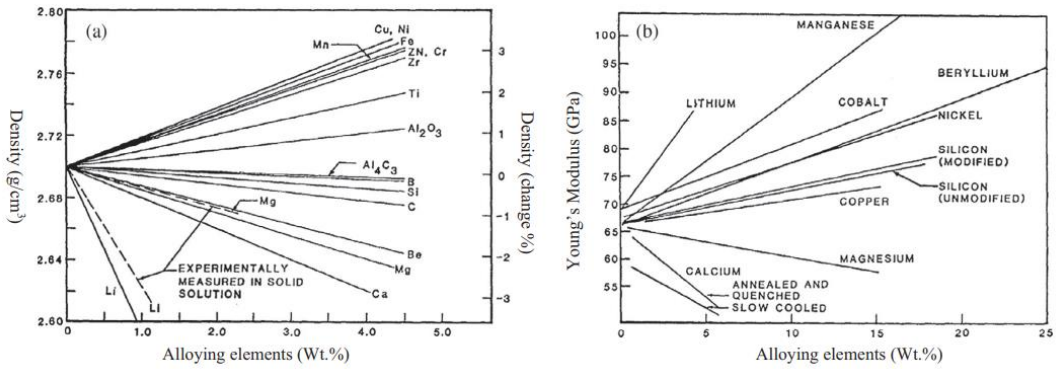

Figure 1.2. The effect of alloying elements on the a) density and b) Young's modulus of aluminum [9].

Due to the difficulties encountered in first-generation Al-Li alloys, second-generation Al-Li alloys have been developed to obtain lighter (8-10%) and stronger alloys compared to conventional aluminum alloys for aerospace and aircraft applications [10]. These second-generation Al-Li alloys have a copper content of less than 2% by weight and lithium concentrations exceeding 2% by weight. The silicon (Si) and iron (Fe) content were minimized to attain high ductility and toughness. Manganese (Mn) was replaced with zirconium (Zr) to produce Al_3Zr precipitates that effectively refine grain structure, increase nucleation voids, and improve ductility and toughness [10,11]. As a result, Alcoa Company has successfully replaced the 7075-T6 alloy with second-generation Al-Li products, including 2090-T86 extrusion, 2090-T83 and T84 sheets, and 2090-T81 sheets. Pechiney Company replaced 2024-T3 alloy plates with 2091-T8X, and British Aerospace replaced 2024-T3 alloy plates with 8090-T81 plates [4,12]. Although these alloys have low density, high modulus of elasticity, and fatigue life, they have the important disadvantage of highly anisotropic mechanical properties [13]. These disadvantages were observed in later studies to result from sharp crystallographic textures, low short transverse properties, crack deviations, and delamination problems during manufacturing. Also, it was reported that the formation of shearable δ (Al_3Li) precipitates leads to planar slip and localized plasticity and causes a negative effect on both the ductility and fracture toughness of the alloy [14,15]. As

a result, the application of second-generation Al-Li alloys was limited to the use of both 2090 and 8090 alloys in the A340 aircraft for C-17 cargo transport, as well as the use of 8090 alloys in the EH101 helicopter [16].

In the 1990s, third-generation Al-Li alloys were developed with reduced Li concentration (Li < 2 wt%) to overcome the aforementioned disadvantages of the first and second-generation Al-Li alloys. Specifically, their lithium concentration was adjusted to 1.3 wt%, where the strength of the alloy peaked [17]. The alloy composition was in the T_1 phase field, and Mg and Ag were added as the nucleation agents for the precipitation of the T_1 phase. Also, Zr was added for control of grain structure. Other alloying elements, such as Zn and Mn, are also used in the third-generation Al-Li alloys, and their effects on the alloy properties are discussed in detail in the following section [18].

The third generation of Al-Li alloys was mainly developed to address the needs of future aircraft, mainly the weight, maintenance, and performance requirements. Examples of third-generation Al-Li alloys include AA2076, AA2065, AA2055, AA2060, AA2050, AA2199, AA2099, AA2397, AA2297, AA2198, AA2196, and AA2195 [19]. Among these alloys, AA2198-T851 was developed for the replacement of AA2524-T3 and AA2024 in aircraft structures due to its lower density and higher fatigue resistance than these alloys [17]. As another example, AA2099 alloys could replace 7xxx, 6xxx, and 2xxx Al alloys in their applications, including fuselage structures and lower wing stringers, which operate under dynamic or static loading. Also, 2199-T8E79 plates and 2199-T8 sheets replaced many other Al alloys (AA2024-T351, AA2324-T39, AA2624-T351, and AA2624-T39 and AA2024-T3, AA2524-T3, and AA2524-T351, respectively) in the structural aircraft parts [17,19].

The Al-Li alloy 2050, which is the primary focus of this study, was designed as a potential replacement for 7xxx and 2xxx alloys. Specifically, the producer, Constellium, indicated that the alloy is developed to replace incumbent plate alloys such as 7050 due to its lower density, higher modulus, and higher corrosion

resistance [20]. According to the producer, Airware®2050 alloy can be used in lower wing structures or heavy gauge parts like frames, beams, spars, or ribs, requiring high strength and toughness levels. The alloy is reported to possess high strength and high damage tolerance together with low density in a thick plate product, being beneficial for weight saving. Property comparison of alloys 2050 and 7050 is shown in Figure 1.3, where the 2050-T84 alloy outperforms 7050-T74 in stress corrosion, fatigue, strength, toughness, density, and stiffness [21].

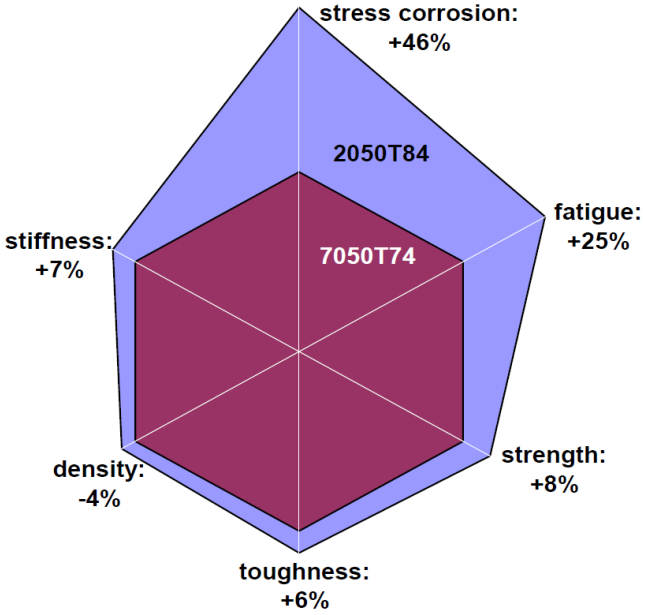

Figure 1.3. Property comparison of aluminum 2050 and 7050 alloys [21].

The following sections provide a comprehensive discussion of the 2050-T84 alloy, covering its chemical composition, the role of alloying elements, secondary phases, and grain structure. The mechanical and physical properties of the alloy are also discussed in detail.

1.2 Chemical Composition of AA2050 Alloy and the Role of Alloying Elements

The chemical composition of the alloy, in accordance with the AMS 4413 standard, is shown in Table 1.1.

Table 1.1 Chemical composition of AA2050 alloy (AMS 4413).

Element	Si	Fe	Cu	Mn	Mg	Cr	Zn	Ti	Zr	Ag	Li
Min	-	-	3.2	0.20	0.20	-	-	-	0.06	0.20	0.70
Max	0.08	0.10	3.9	0.50	0.60	0.05	0.25	0.10	0.14	0.70	1.30

The lithium content of the alloy is set to between 0.7 – 1.3 wt.%. The lithium content was set to a maximum of 1.3 wt.% to avoid δ' (Al3Li) phase formation, which is detrimental to thermal stability. The copper content of the alloy was adjusted to 3.2 – 3.9 wt.% so that high strength and toughness could be achieved. The main strengthening phase in this copper and lithium content is the T_1 phase (Al_2CuLi). The addition of the limited amount of Mg and Ag was due to the nucleation and growth of this phase. Dislocations generated due to the cold work prior to artificial aging also favored the nucleation and growth of the T_1 phase [22]. T_1 precipitates, having a plate-like shape and a hexagonal crystal structure (a = 0.4965 nm and c = 0.9345 nm), are reported to precipitate on {111} [16]. TEM image of the T_1 precipitates is shown in Figure 1.4 [20].

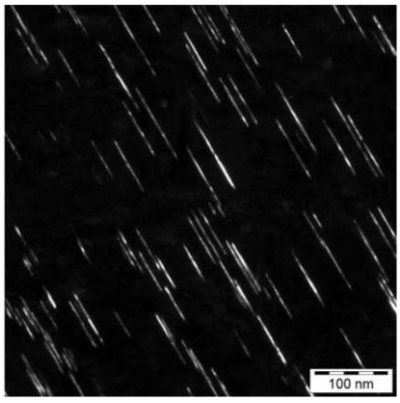

Figure 1.4. TEM image of the T_1 precipitates [20].

Mn and Zr precipitate as dispersoids and help to achieve an unrecrystallized structure. SEM images of Mn-containing dispersoids and Al_3Zr dispersoids are shown in Figure 1.5. Al_3Zr precipitates are coherent and have spherical shapes. They are reported to be stable due to low solid solubility of Zr in Al and a small misfit between the precipitate and the matrix. They effectively pin the grain and subgrain boundaries, providing an unrecrystallized structure [4, 20].

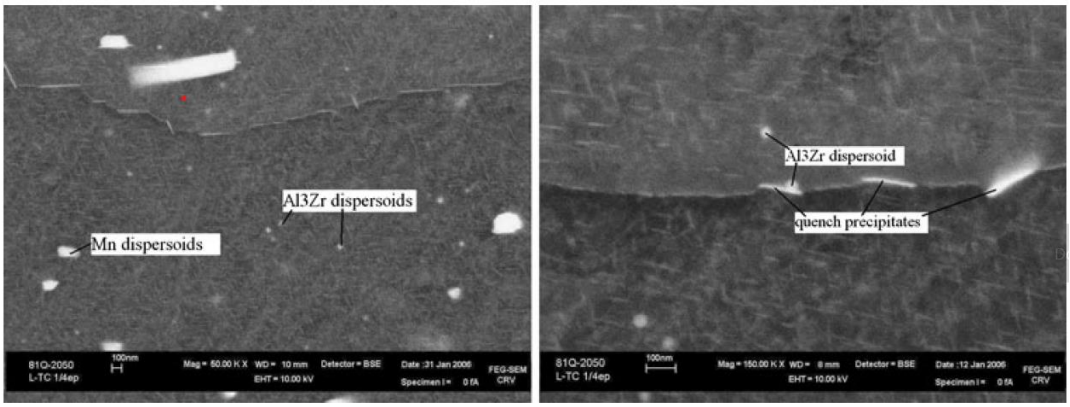

Figure 1.5. SEM images of Mn-containing dispersoids and Al_3Zr dispersoids [20].

It is also worth noting that aluminum alloys contain impurities such as iron and silicon. During the ingot solidification and subsequent processing, these impurities precipitate as insoluble phases and cause detrimental effects on the ductility and fracture toughness of the alloy. Therefore, the Fe and Si content of the modern aluminum-lithium alloys is decreased to prevent their negative effect on the alloy ductility and toughness. That said, zinc is another important alloying element of AA2050 alloy that substantially improves its corrosion resistance [23].

1.3 Microstructure of the AA2050 Alloy

The typical microstructure of the AA2050 alloy consists of elongated and lamellar grains as a result of the rolling process. Also, it was reported that the aspect ratio of the grains increases as the plane thickness decreases. This was attributed to the higher amount of rolling to decrease the plate thickness. For instance, the NASA report published in 2011 compared the through-thickness microstructures of two plates

having thicknesses of 2 and 4 inches, as shown in Figure 1.6 and Figure 1.7, respectively. Largely non-recrystallized microstructure having elongated grains along the rolling direction are apparent for both plates. Grain dimensions were reported as 500, 200, and 50 μm, in L, T, and S directions, respectively, for the 4-inch plate [24].

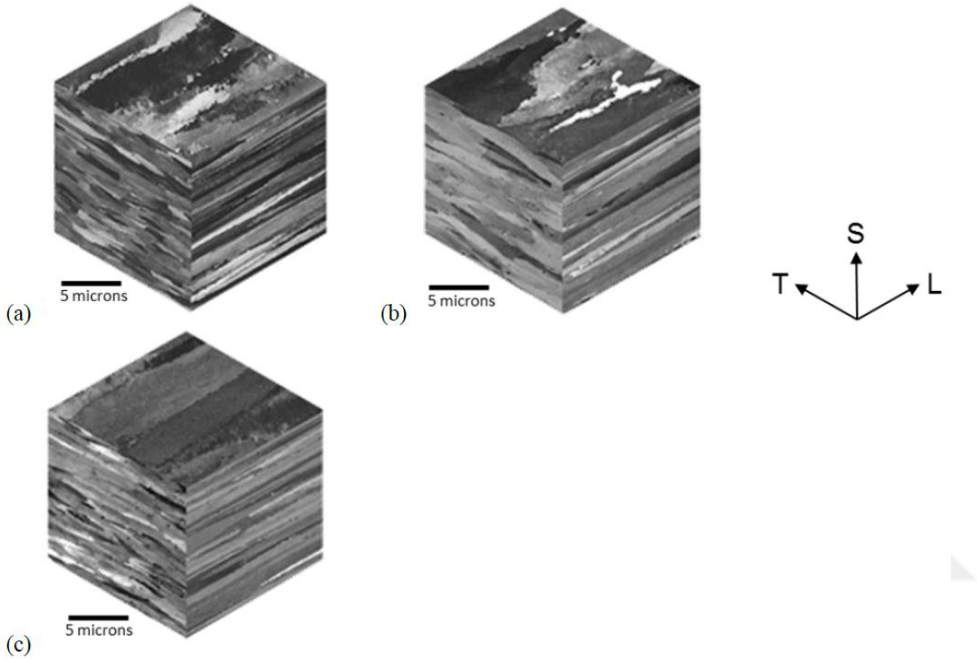

Figure 1.6. Optical microscope images of 2 inch thick AA2050-T84 plate obtained from through-thickness locations of a) t/6, b) t/2, and c) 5t/6 [24].

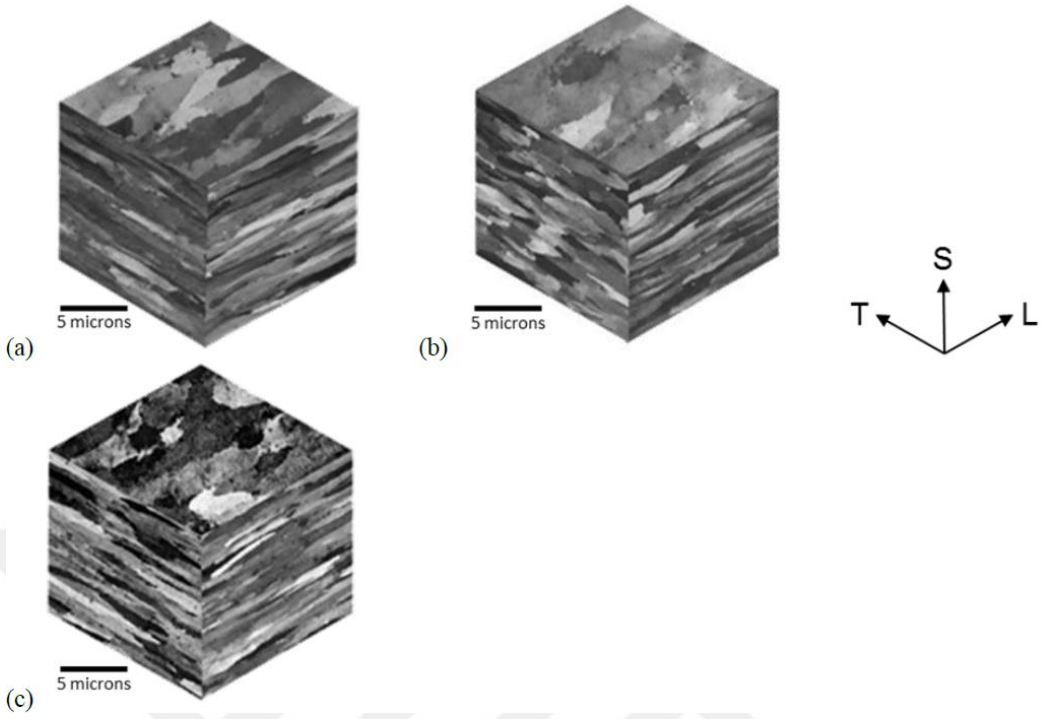

Figure 1.7. Optical microscope images of 4 inch thick AA2050-T84 plate obtained from through-thickness locations of a) t/6, b) t/2, and c) 5t/6 [24].

In another study, Esin et al. [25]. characterized the microstructure of Constellium AA2050 alloy of 100 mm thickness by electron backscatter diffraction. Their result that displays the 3D grain structure of the alloy is shown in Figure 1.8. Grains are elongated in the rolling direction with an aspect ratio of 10. Also, their measurements exhibited a mean grain size ranging between 30 and 300 μm. Their findings showed that the alloy was in a non-recrystallized state.

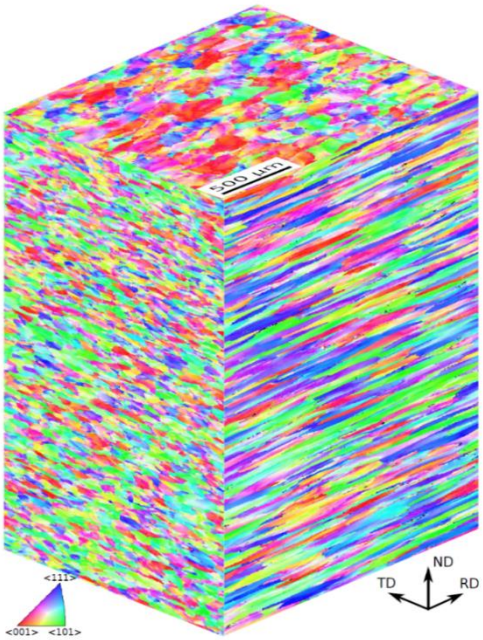

Figure 1.8. 3D orientation map of Constellium AA2050 alloy [25].

Intermetallic inclusions are also present in the microstructure of AA2050 alloy. These inclusions can be divided into two groups, Fe-rich and Mn-rich. Apparently, they are formed on the grain boundaries and elongated in the rolling direction, as shown in Figure 1.9. Also, it was reported that the Fe-rich inclusions were larger than the Mn-rich inclusions.

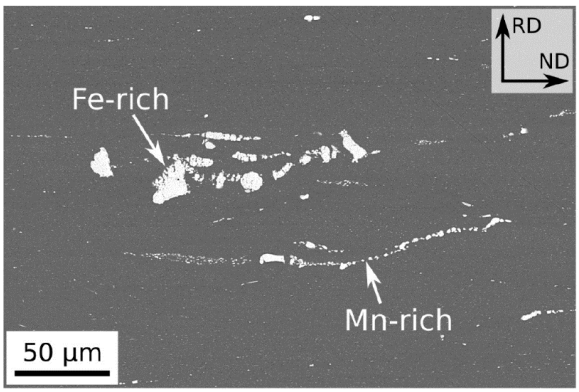

Figure 1.9. Backscattered SEM image of Fe and Mn containing inclusions in AA2050-T84 alloy [25].

1.4 Mechanical Properties of AA2050-T84 Alloy

Strength-ductility relationships demonstrated for various types of Al-Li alloys are shown in Figure 1.10. The best performance is achieved for the Al-Li alloys that contain Cu, Mg, and Zr, which are the alloying elements present in the third generation of Al-Li alloys, including 2050 alloy [6].

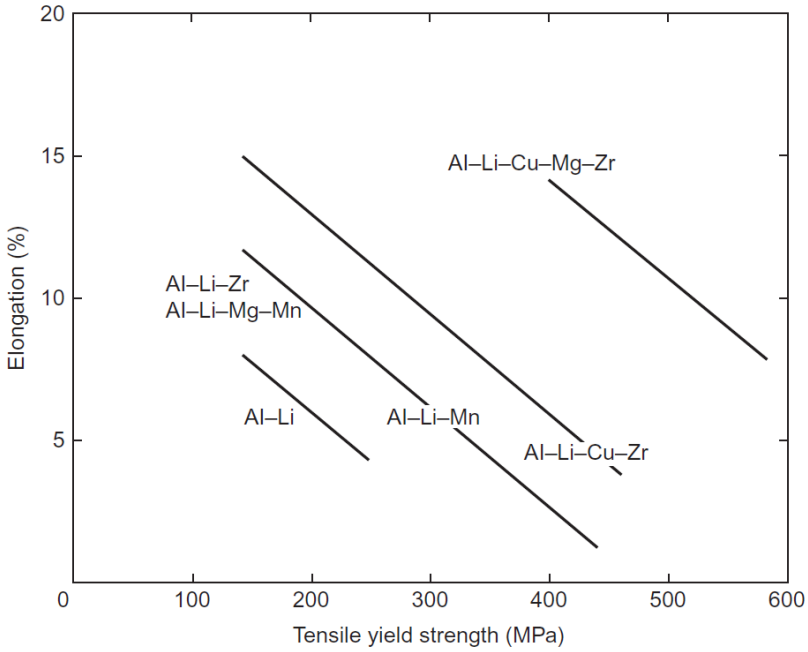

Figure 1.10. Comparison of the %elongation and yield strength ranges of different Al-Li alloys [6].

The tensile properties of the AA2050 alloy are investigated by several studies in the literature. Their results suggest that the yield strength, tensile strength, and the % elongation values of the alloy differ depending on the plate thickness, sample orientation, and position. For instance, the results of Lu et al. [27] exhibited the anisotropic nature of the alloy. Their results were obtained from an 80 mm thick plate, and listed in Table 1.2. Tensile strength, yield strength, and the % elongation of the alloy range between 549-599 MPa, 504-570 MPa, and 5.5-12.2%, respectively.

The high yield strength of the AA2050 alloy is mainly attributed to precipitation strengthening. However, it was also shown as one of the reasons for the inhomogeneous mechanical properties of the alloy. The rolling texture and the anisotropic grain structure of the alloy are among the other important factors causing inhomogeneous mechanical properties.

Table 1.2 Tensile test results of an 80 mm thick plate AA2050 alloy [24].

Plate Thickness (mm)	80					
Position	t/6		t/3		t/2	
Orientation	L	LT	L	LT	L	LT
Tensile Strength (MPa)	549	558	557	556	599	558
Yield Strength (MPa)	523	517	528	504	570	510
% Elongation	12.2	6.8	11.8	6.6	10	5.5

Hafley et al. [24] carried out tensile tests using specimens extracted from a 100 mm thick plate. Specimens were extracted from 4 principal planes (L, LT, ST, and 45o) and two different positions (t/6 and t/2). Their results are listed in Table 1.3. Tensile strength, yield strength, and % elongation values were in the range of 502-546 MPa, 443-514 MPa, and 4.8-13.8%, respectively. These results also indicate the anisotropic mechanical properties of the alloy

Table 1.3 Tensile test results of a 100 mm thick plate AA2050 alloy [24].

Plate Thickness (mm)	100							
Orientation	L		LT		ST		45	
Position	t/6	t/2	t/6	t/2	t/6	t/2	t/6	t/2
Tensile Strength (MPa)	510	546	522	516	-	505	502	499
Yield Strength (MPa)	487	514	480	468	-	443	451	452
% Elongation	13.8	8.8	11.3	8.5	-	4.8	12	9.9

The mechanical properties of 2050-T84 are compared with conventionally used 7050-T7451 plates having different thicknesses, such as 25, 38, and 100-125 mm, in Table 1.4. The table clearly shows that 2050-T84 demonstrates enhanced strength and toughness values together with a lower density than the 7050-T7451 [20].

Table 1.4 Comparison of the mechanical and physical properties of 2050-T84 and 7050-T7451 [20].

Thickness		25-38 mm		100-125 mm	
Alloy		7050-T7451	2050-T84	7050-T7451	2050-T84
Basis		A-value	S-value	A-value	S-value
UTS, (MPa)	L	510	503	490	490
	LT	510	510	490	490
	ST	…	…	462	476
σ_y (MPa)	L	441	476	421	455
	LT	441	462	421	441
	ST			393	407
KIc, MPa√m	L-T	29	36	27	28
	T-L	25	32	24	23
	S-L	…	…	23	23
E (GPa)		69	76.5	69	76.5
q (g/cm3)		2.83	2.70	2.83	2.70

1.5 Fatigue Crack Growth Behavior of AA2050 Alloy

The fatigue crack growth behavior of the AA2050 alloy holds paramount significance as it was intended to be used in aerospace applications. In the aerospace industry, materials are subjected to demanding cyclic loading conditions during flight cycles. Therefore, understanding how fatigue cracks propagate within the AA2050 alloy is of crucial importance. FCG behavior of metallic materials depends on grain size and

orientation, precipitate size and distribution, texture, and loading geometry [28]. It is important to analyze the interplay between these factors and the FCG behavior of the alloy for safer and more reliable aerospace operations.

There are several studies in the literature investigating the FCG behavior of AA2050 alloy. For instance, Cavalcante et al. [29] studied the effect of orientation on the FCG behavior of AA7050 and AA2050 alloys. Their results suggested that AA2050 alloy exhibited better FCG performance than the AA7050 alloy (Figure 1.11). The better resistance to crack propagation in Al-Li alloys under conditions of consistent amplitude can be attributed to the promotion of planar shear behavior facilitated by the presence of consistent and shearable precipitates within the structure of the alloy [30]. Furthermore, investigations have reported that the AA2050-T84 alloy exhibited a crystallographically verified propagation path situated on (111) planes or in close proximity to such surface facets. The occurrence of planar slip phenomena has been observed to induce crack branching, an elongated total crack path, and a reduction in the effective stress intensity at the crack tip, collectively contributing to the reducing of crack growth rate [31,32].

The orientation of the specimens exhibited minimal effect on the fatigue crack growth rate (FCGR) for both alloys. There was a slight improvement in FCGR observed for specimens oriented in the longitudinal-transverse (L-T) direction. Given the elongated of the grain structures, the transverse-longitudinal (T-L) orientation facilitated crack growth primarily along the grain boundaries with minor deviations. In contrast, "barrier effect" at the grain boundaries, leading to a slight reduction in FCGR in the L-T orientation [33].

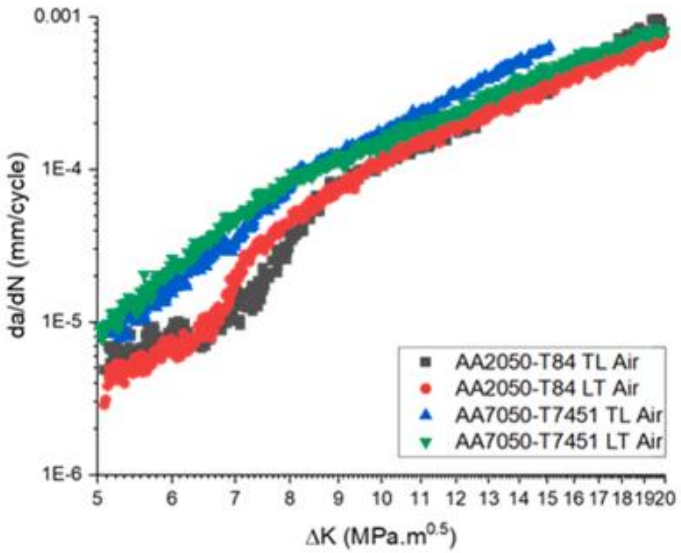

Figure 1.11. Effect of orientation on the FCG behavior of AA2050-T84, and AA7050-T7451 alloy [29].

In another study, fatigue crack deviation was observed in a 100 mm thick AA2050-T84 alloy, when the loading direction was parallel to rolling direction (RD) as show in Figure 1.12 [25]. Formation of micro-cracks perpendicular to the principal crack growth direction path was reported. Also, weakened GBs due to precipitate free zones were shown to contribute crack path deviation.

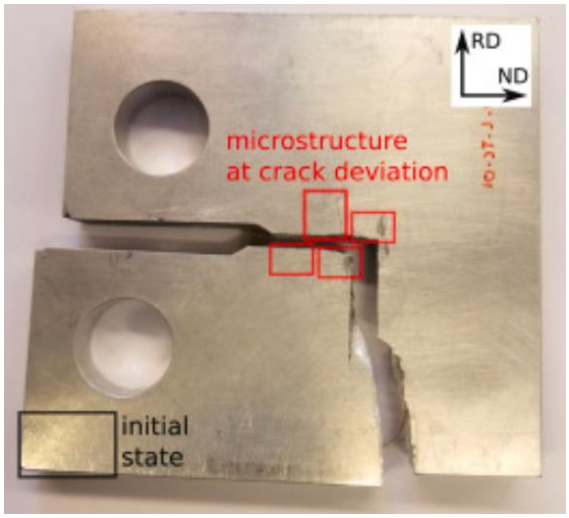

Figure 1.12. Fatigue crack deviation in AA2050-T84 alloy. [25].

1.6 Aim of the Study

The aim of this study can be dived into four different parts as follows. Firstly, a thorough exploration of the anisotropic microstructure of the AA2050 alloy induced by the hot rolling process will be undertaken. This will be achieved through metallographic and crystallographic characterizations of 20 mm and 130 mm thick plates, which underwent same production stages with different extent of hot rolling. The second aspect involves an in-depth assessment of the effect of grain anisotropy, aspect ratio and elongation on the mechanical properties. This evaluation will include tensile tests, hardness measurements, impact tests and high-cycle fatigue tests. The study also entails the execution of fatigue crack growth tests coupled with a detailed fractographic analysis, shedding light on the fracture mechanisms and behavior. Lastly, a significant endeavor involves the correlation of microstructure and texture with crack path deviation, specifically in the 20 mm thick plate. Collectively, this study aimed to establish a comprehensive understanding of the interplay between processing, microstructure, mechanical properties, and crack propagation behavior in the AA2050 alloy, ultimately contributing to the existing body of literature and application especially for aerospace applications.

CHAPTER 2

EXPERIMENTAL PROCEDURE

2.1 Material

The AA2050-T84 alloy utilized in this research was provided by Turkish Aerospace Industries and sourced as a plate from Constellium in France. The chemical composition of the alloy, in accordance with the AMS 4413 standard, is shown in Table 1.1. AA2050 alloy having 20 and 130 mm thick plates were investigated in this study. The thickness of the plates was reduced to the aforementioned values by hot rolling process starting from the same thickness. Therefore, the extent of the hot rolling prosess was higher for 20 mm thick plate. T84 heat treatment which includes solution heat treatment, cold deformation, and artificial aging steps subsequently was applied to the both plates to improve their mechanical properties. Samples were extracted from the center of thickness location (t/2) of the 20 mm thick plate and the mid-thickness location (t/4) of the 130 mm thick plate. A comparative analysis between the two thicknesses aimed to understand how the rolling operation for achieving thin plates influences the microstructure and overall mechanical performance of the alloy.

2.2 X-ray Fluorescence (XRF) Measurements

X-Ray Fluorescence (XRF) measurements were conducted using Bruker S1 Titan X-ray fluorescent (XRF) analyzer to confirm the composition of the alloy matches AA2050 composition reported in AMS 4413.

2.3 Metallographic Examinations

Metallographic examinations were carried out using samples extracted from 20 mm and 130 mm thick blocks. LT-ST, L-ST and L-LT planes were investigated for each sample where the longitudinal direction (L) represents the rolling direction and the width and the thickness of the plate are named as the long transverse direction (LT), and the short transverse direction (ST), respectively. Sample preparation was carried out as per ASTM E3, which includes cutting, mounting, grinding, polishing, and etching, respectively. The cutting process was carried out using the ATM Brillant 220 cutting device. Subsequently, all samples were bakelite embedded using Metkon Ecopress-100 mounting press. Grinding and polishing was carried out using Struers Tegramin-25 grinding and polishing device. Then, specimens are etched using Keller's reagent with a composition given in ASTM E407 – 07 standard.

Microstructural investigations of surfaces etched with Keller's reagent was performed using Leica DM2700M optical microscope and Olympus GX53 inverted optical microscope. Average grain size and aspect ratio measurements were carried out using the intercept method on ImageJ program according to ASTM E112.

The second phase particle analysis was performed automatically by the LASX Software connected to Leica optical microscope, following the ASTM E1245 standard. As-polished surfaces were used in this analysis. To make the secondary particles more apparent, the surfaces underwent an extended polishing duration of an additional 2 minutes beyond the usual preparation time using colloidal silica. Detailed investigations were made using the ZEISS Sigma 300 scanning electron microscope (SEM).

2.4 X-ray Diffraction (XRD) Analysis

X-ray diffraction (XRD) patterns of samples (15 mm × 10 mm × 3 mm) were obtained using a Rigaku D/Max-2200 x-ray diffractometer. Samples were cut from 20 and 130-mm thick plates in 3 different orientations so that XRD patterns were

obtained from L-LT, L-ST, and LT-ST planes. Scans were taken with monochromatic Cu Kα radiation (λ = 1.54 Å) at 40 kV at diffraction angles (2θ) ranging from 10^o to 120^o at a scanning rate of 2^o min^{-1}.

2.5 Hardness Test

Hardness tests were carried out according to the ASTM E92 standard using Qness Q10A+ microhardness test machine. HV10 test method (Vickers hardness, 10 kgf for 15 seconds) was performed on polished specimens in three directions for each sample. 5 different indentations were used for each measurement.

2.6 Tensile Test

Tensile tests were performed to determine the yield strength, tensile strength, and Young's modulus of the alloy. The tests were carried out using an INSTRON 5985 with a load capacity of 250 kN, following the ASTM E8 standard. A 12.5 mm long extensometer (INSTRON 2620-601) with a deformation rate of 0.015 (mm x mm^{-1} x min^{-1}) was used. The extensometer was not removed from the samples until the end of the test. Elongations were measured manually for each sample after the test was completed.

Round-type tension test specimens were prepared according to ASTM E8. Drawings of the samples are shown in Figure 2.1. Samples extracted from the 20 mm and 130 mm thick plates have 6 mm (subsize) and 12.5 mm (standard) gauge diameters, respectively. Six samples were tested from three directions for each plate.

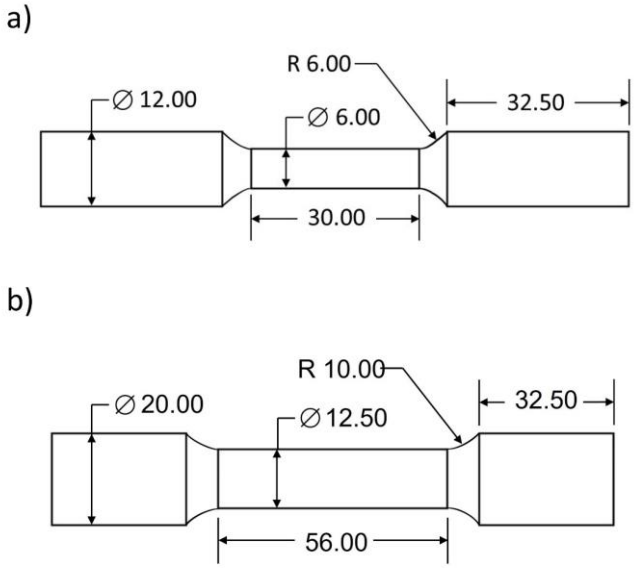

Figure 2.1. Schematic drawing of a) subsize and b) standard tension test specimens.

The tensile test samples were obtained from the center of thickness (t/2) of the 20 mm thick plate. The orientation of the samples was L, LT and 45 degrees with respect to the rolling direction. The samples from the 130 mm thick plate were obtained from the t/4 location and had two orientations: L and LT. Sample directions and locations are shown in Figure 2.2.

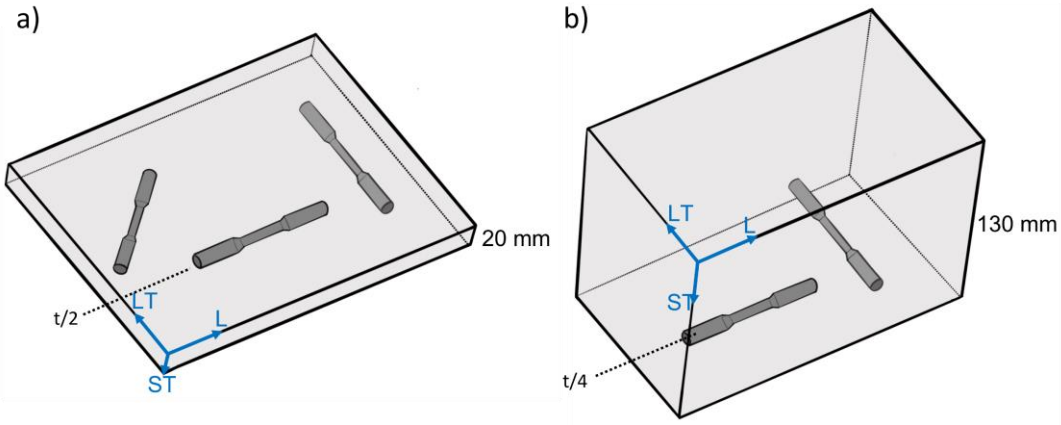

Figure 2.2. Schematic drawings showing the locations and orientations of tensile test samples extracted from a) 20 mm and b) 130 mm thick plate.

2.7 High Cycle Fatigue (HCF) Test

Fatigue tests were performed according to ASTM E-466 standard to generate S-N curves for the samples extracted from the t/2 and t/4 locations of 20 mm and 130 mm plates, respectively. 27 samples were tested for P20_L, while 20 samples were tested for P20_LT. Also, 12 specimens were tested to construct the S-N curve for P130_L, and 14 specimens were tested for P130_LT. All fatigue tests were carried under constant amplitude cyclic loading with a stress ratio (R) equal to 0.1. The fatigue loads were applied in the form of a sinusoidal wave and frequency of 80-100 Hz using RUMUL Magnetic Resonant Test Machine. Fatigue test specimen geometries are given in Figure 2.3. The HCF test specimens with a gauge diameter of 5.8 and 8 mm were used for the 20 and 130 mm thick plate, respectively. The parameters b_0 and b_1 in Equation 1, representing the coefficients of the linear model, were calculated according to ISO 12107 and S-N curves were constructed accordingly.

$$log(N) = b_0 + \ b_1 log(S) \tag{1}$$

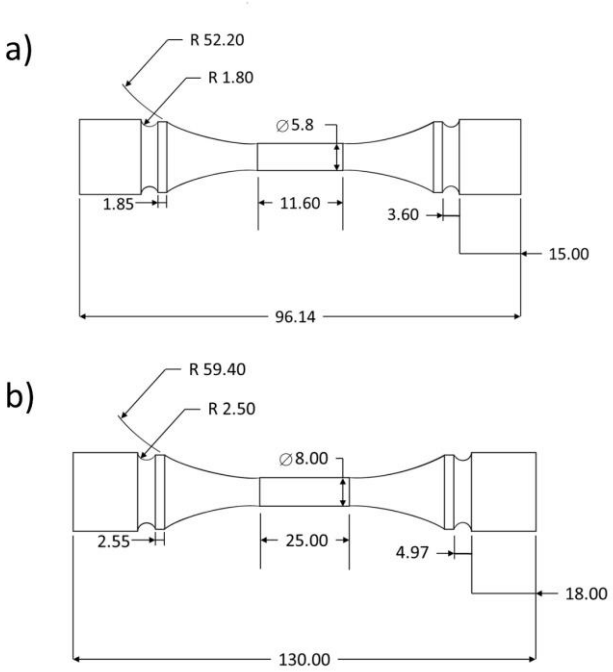

Figure 2.3. High cycle fatigue test specimen geometries with a gauge diameter of a) 5.8 and b) 8 mm.

2.8 Charpy Impact Test

The Charpy impact test was carried out according to ASTM E23 standard using Charpy test specimens on a pendulum-type Tinius Olsen impact tester. The tests were conducted at room temperature. The V-notch Charpy impact specimens were prepared in both the rolling direction (L) and transverse direction (LT) of 20 mm and 130 mm plates with dimensions 55 x 10 x 10 mm (Figure 2.4). The specimens had a 45-degree V-notch with a depth of 2 mm and a radius of 0.25 mm. Sample directions and locations are shown in Figure 2.5. Each test condition was evaluated through a single test.

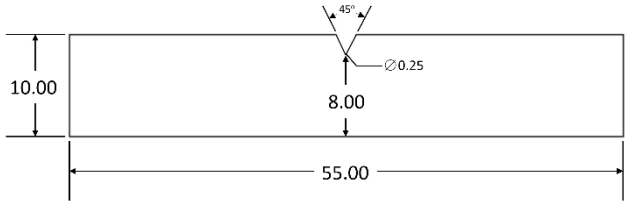

Figure 2.4. Schematic drawing of the Charpy impact test specimen.

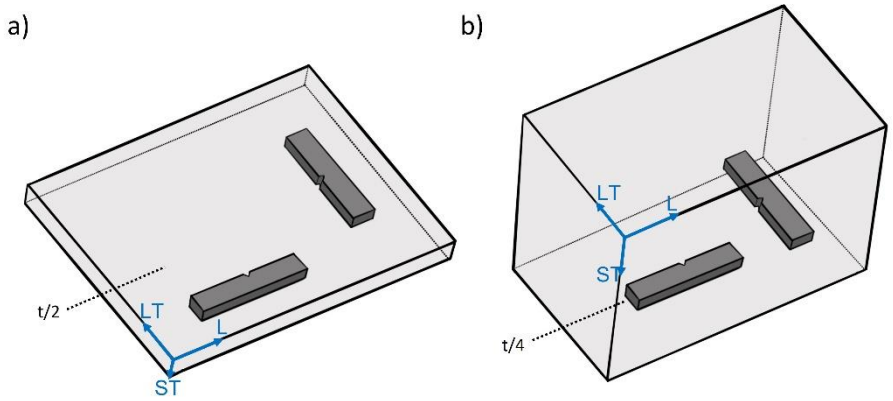

Figure 2.5. Schematic drawings showing the locations and orientations of Charpy impact samples extracted from a) 20 and b) 130 mm thick plate.

2.9 Fatigue Crack Growth (FCG) Test

FCG tests were performed according to ASTM E647. The tests are performed by a INSTRON 8803 servo-hydraulic machine. Firstly, pre-cracking is performed with constant ΔK and the crack is opened until reaching the notch size. After pre-cracking, Paris section is started just above the pre-crack ΔK and test is performed under constant loading. The specimens are loaded at R = 0,1. A sinusoidal waveform was applied at a loading frequency of 10 Hz. W=60 compact tension (CT) samples were used in the tests. Technical drawing of CT samples prepared according to related standard were given in Figure 2.6. These specimens are extracted from the t/2 location of 20 mm thick plate and t/4 location of 130 mm thick plate as shown in the schematic drawings. Also, two different orientations are selected to investigate the effect of orientation as shown in Figure 2.7.

CT specimens were sampled in the L-LT plane of each plate. The load was applied in T direction and the crack was aligned with the L direction for three specimens extracted from each 20 mm and 130 mm thick plate. Also, load was applied in L direction and the crack was aligned with the T direction for two specimens extracted from each 20 mm and 130 mm thick plate.

The stress intensity factors for each specimen type are determined through the utilization of the relevant calculations specified in ASTM E647. Crack Opening Displacement (COD) method was utilized for crack size measurements and the calculations were done following the front-face compliance method in ASTM E674. In cases where the crack opening displacement (COD) measurements yield an excessive amount of data due to noise, a filtering process is employed to refine and eliminate such data points. After the pre-crack and Paris sections, crack size measurements were carried out under optical microscope to assess and correct the raw datasets obtained from the testing machine. After these corrections, the da/dN calculation tool internally employs the Incremental Polynomial Method (7^{th} degree) in accordance with the guidelines specified in ASTM E647.

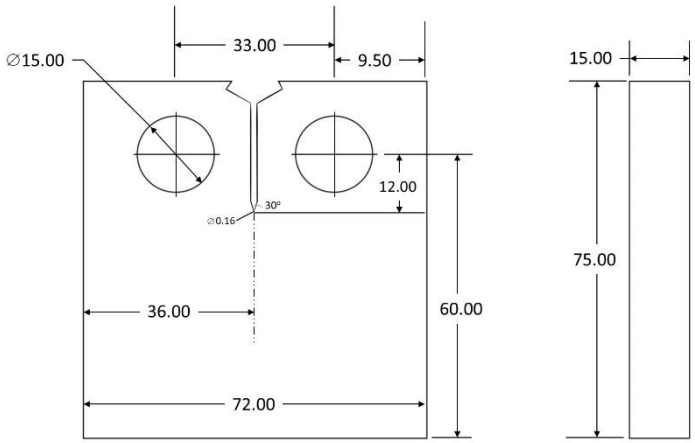

Figure 2.6. Schematic drawing of the W=60 compact tension (CT) specimen.

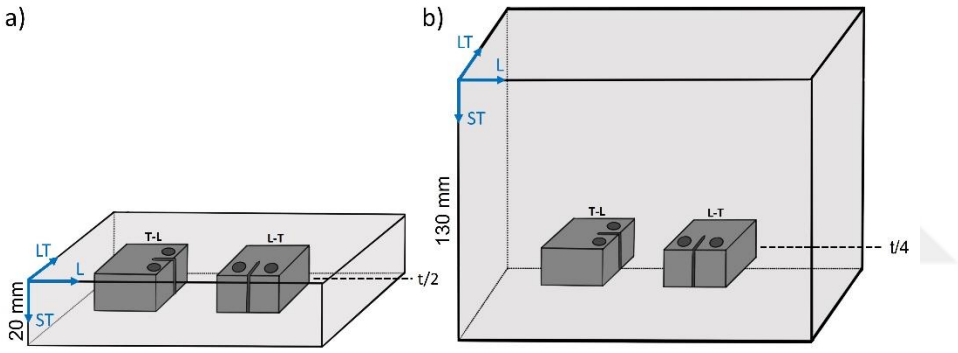

Figure 2.7. Schematic drawings showing the locations and orientations of CT samples extracted from a) 20 mm thick plate and b) 130 mm thick plate.

2.10 Fractographic Analysis

Fractographic analysis of the test specimens was carried out using the ZEISS Sigma 300 scanning electron microscope (SEM). Detailed investigations were made using secondary electron detectors. Also, macro examinations of the fractured surfaces were carried out using the NIKON SMZ745T stereo microscope.

2.11 EBSD Analysis

The analysis of electron backscatter diffraction (EBSD) of the LT-ST planes of the specimens extracted from 20 mm (t/2 location) and 130 mm plates (t/4 location) was carried out using FEI Nova Nano scanning electron microscope (SEM) at an accelerating voltage of 20 kV, with a scanning step size of 40 μm. Prior to EBSD analysis, specimens were grinded and polished manually. In the final step, 40 nm colloidal silica was used to prepare a mirror-finish surface. The acquired EBSD data was subsequently analyzed using the TSL OIM data collection software.

CHAPTER 3

RESULTS AND DISCUSSION

3.1 X-ray Fluorescence (XRF) Measurements the Alloy

Chemical composition of the alloy was characterized by XRF. The results are reported in Table 3.1 and compatible with the AMS 4413. Due to the low-energy X-ray emission characteristic of lithium (Li), it was not detected because it fell below the sensitivity range of the detector used.

Table 3.1 XRF results of the AA2050 alloy (wt%).

Element	Si	Fe	Cu	Mn	Mg	Cr	Zn	Ti	Zr	Ag	Al
wt%	0.03	0.07	3.68	0.37	0.31	0.02	0.17	0.03	0.08	0.39	Base

3.2 Microstructural Examination

Microstructural analyses of the samples were conducted in three different directions for both 20 mm and 130 mm thick plates: the longitudinal direction (L-LT), the long transverse direction (LT-ST), and the short transverse direction (L-ST). Optical microscopy was used for the characterization of the samples' grain structure. 3D illustration of the microstructure of the 20 mm thick plate is given in Figure 3.1. Also, micrographs of three different directions captured by with 1.25X, 2.5X, 5X lenses are given in Figure 3.2. The microstructure consists of elongated grains aligned with the rolling direction. Second phase particles were also observed to be oriented in the rolling direction.

The average grain length and width measured for L-LT, L-ST and LT-ST planes of the 20 mm thick plate samples are reported in Table 3.2. The results showed that grain size of the plate differ significantly with respect to its planes. The largest grains were observed on the L-LT plane having an average grain length of 2942 ± 1148 μm

and grain width of 557 ± 215 μm, yielding an aspect ratio of 5. On the L-ST plane both the grain length and width were smaller than the L-LT plane with an average grain length and width of 2476 ± 1229 and 93 ± 42 μm, respectively. The grains are extremely elongated along L direction in the L-ST plane. This plane has the grains with the highest aspect ratio (27) among all planes which is apparent in Figure 9b. The grains on the LT-ST planes had an average grain length and width of 345 ± 122 and 40 ± 25 μm, respectively, with an aspect ratio of 9. The optical micrographs and the measured grain sizes showed that the 20 mm thick sample is highly anisotropic in all directions.

Figure 3.1. 3D microstructure of the sample extracted from the 20 mm thick plate.

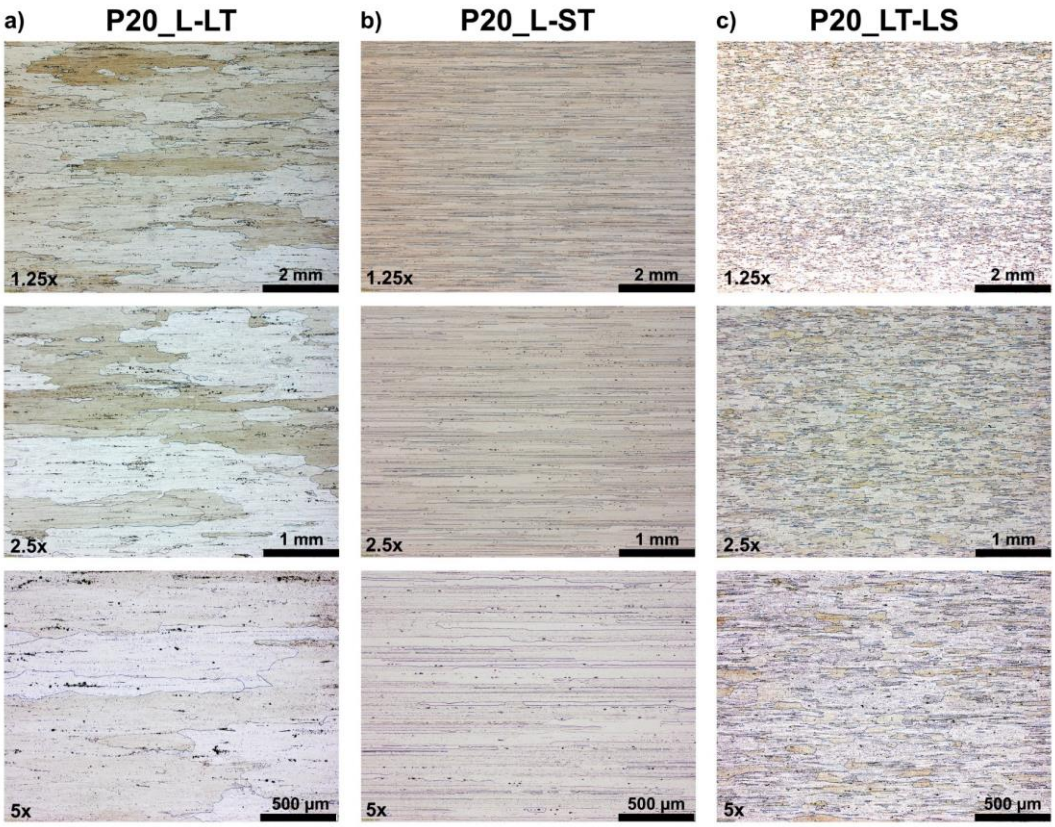

Figure 3.2. Optical micrographs of the a) P20_L-LT b) P20_L-ST, and c) P20_LT-ST.

Table 3.2 Grain size measurements of the sample extracted from the 20 mm thick plate.

	Measured Dimensions		
Plane	Avr grain length, µm	Avr grain width, µm	Aspect ratio
L-LT	2942 ± 1148	557 ± 215	5
L-ST	2476 ± 1229	93 ± 42	27
LT-ST	345 ± 122	40 ± 25	9

In Figure 3.3, a 3D illustration of the microstructure of the 130 mm thick plate is shown. Figure 3.4 shows micrographs taken using 1.25X, 2.5X, and 5X lenses. These micrographs were used for a detailed examination of the plate's grain characteristics.

The average grain length and width values for the 130 mm thick plate was measured for L-LT, L-ST and LT-ST planes. Results are reported in Table 3.3. The L-LT plane exhibited an average grain length of 627±227 μm and a grain width of 149±149 μm, resulting in an aspect ratio of 4. The L-ST plane displayed an average grain length (625±196 μm) similar to L-LT plane and an average width (67±17 μm) smaller than the L-LT plane. This plane showed the highest aspect ratio (9) among all planes, as depicted in Figure 9b. Based on the analysis of the results, it is observed that the L-LT and L-ST planes exhibit similar mean grain lengths, but have slightly different grain widths. For the LT-ST plane, the grains were comparatively smaller than the other planes, with an average grain length of 202 ± 56 μm and a grain width of 68 ± 19 μm, giving an aspect ratio of 3.

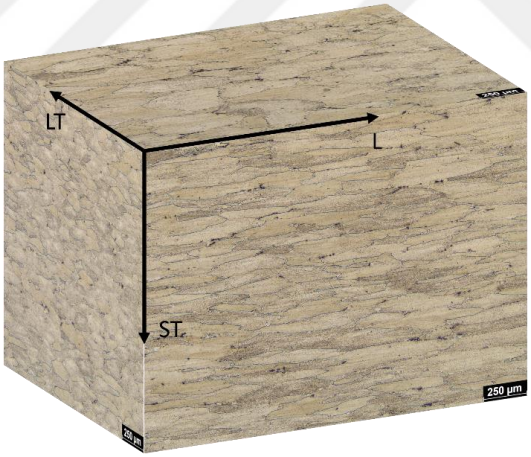

Figure 3.3. 3D visualization of the microstructure in the specimen extracted from the 130 mm thick plate.

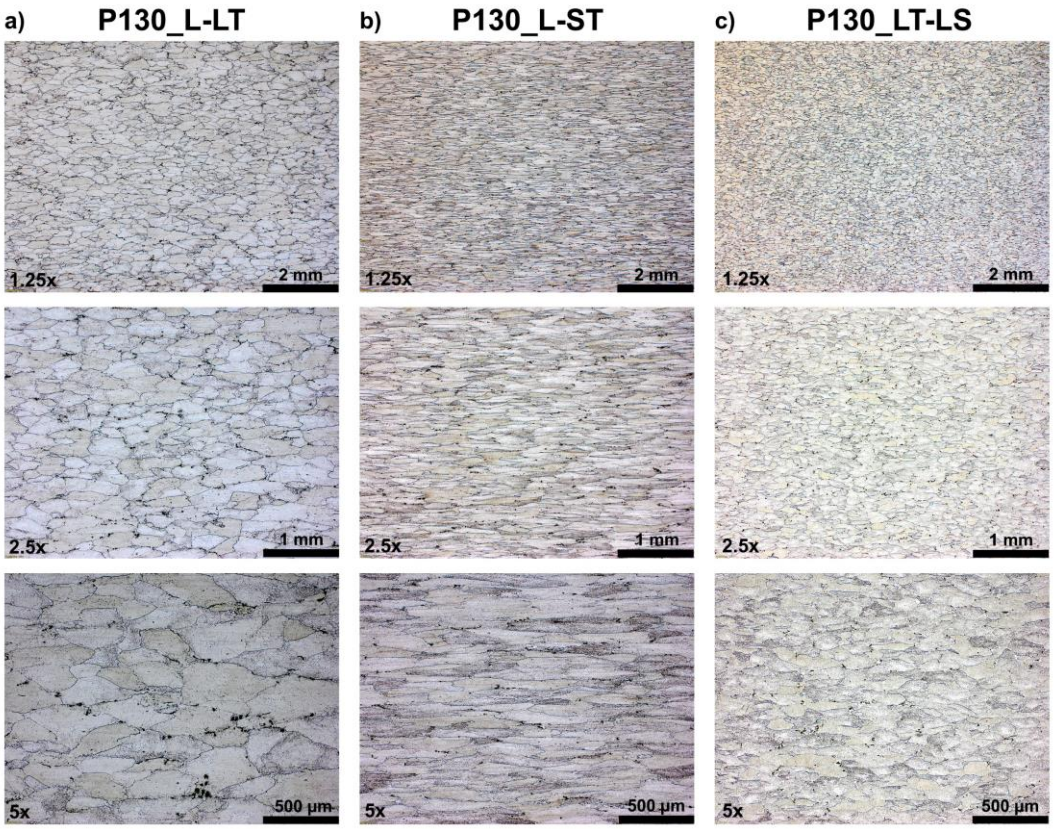

Figure 3.4. Optical micrographs of a) P130_L-LT b) P130_L-ST, and c) P130_LT-ST.

Table 3.3 Grain size measurements of the sample extracted from the 130 mm thick plate.

	Measured Dimensions		
Plane	Avr grain length, µm	Avr grain width, µm	Aspect ratio
L-LT	627 ± 227	149 ± 48	4
L-ST	625 ± 196	67 ± 17	9
LT-ST	202 ± 56	68 ± 19	3

The images of the as-polished surfaces of the 20 mm and 130 thick mm plates in three directions are given in Figure 3.5 and Figure 3.6, respectively.

The optical micrographs of L-LT and L-ST planes of the 20 mm thick plate showed that the second phase particles are highly elongated in the rolling direction whereas they appeared to be slightly elongated on the LT-ST plane. This result was in good agreement with the grain structure of the planes. Large grains are highly elongated in the rolling direction on L-LT and L-ST planes (Figure 3.2a and Figure 3.2b, respectively). As the most of the second phase particles are located on the grain boundaries, they were also elongated in the rolling direction. The grain elongation was lower on the LT-ST plane compared to the other planes which resulted in a less oriented appearance of the second phase particles on the LT-ST plane.

The area percent values of the second phase particles in 20 mm thick plate for L-LT, L-ST, and LT-ST planes were measured as 0.40, 0.46, and 0.23%, respectively (Table 3.4). The smaller percentage area of second phase particles on the LT-ST plane compared to the L-LT and L-ST planes can be attributed to the rolling direction (L) of the plate. Since the grains and, in turn, the second phase particles are elongated in the rolling direction, it is reasonable to expect to observe a greater quantity of particles on the L-LT and L-ST planes than on the LT-ST plane.

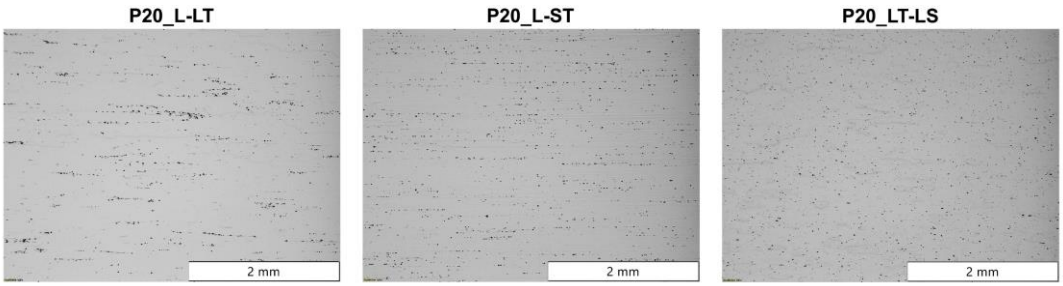

Figure 3.5. Optical microscopy images of the as-polished surface of the 20 mm thick plate obtained from three directions.

The as-polished images of the 130 mm plate revealed a similar trend to the 20 mm plate, where the second phase particles in the L-LT and L-ST planes exhibited elongation along the rolling direction, while appearing slightly elongated in the LT-

ST plane. This observation correlated well with the grain structure of the respective planes. As the majority of second phase particles were situated at the grain boundaries, they exhibited elongation along the rolling direction. Notably, the LT-ST plane displayed lower grain elongation compared to the other planes, resulting in a relatively less oriented appearance of the second phase particles within this plane. The area percentage values of the second phase particles in the 130 mm thick plate were measured as 0.64%, 0.61%, and 0.34% for the L-LT, L-ST, and LT-ST planes, respectively (Table 3.4). Similar to the 20 mm thick plate, the reason for the lower area percent value of the second phase particles on the LT-ST plane compared to the L-LT and L-ST planes can be attributed to the rolling direction (L) of the plate. Due to the elongation of grains and subsequently the second phase particles in the rolling direction, it is reasonable to expect a higher quantity of particles on the L-LT and L-ST planes as compared to the LT-ST plane. Also, it was observed that the second phase particles were less cracked in 130 mm thick plate than 20 mm thick plate. This outcome was attributed to the more extensive rolling process implemented on the latter.

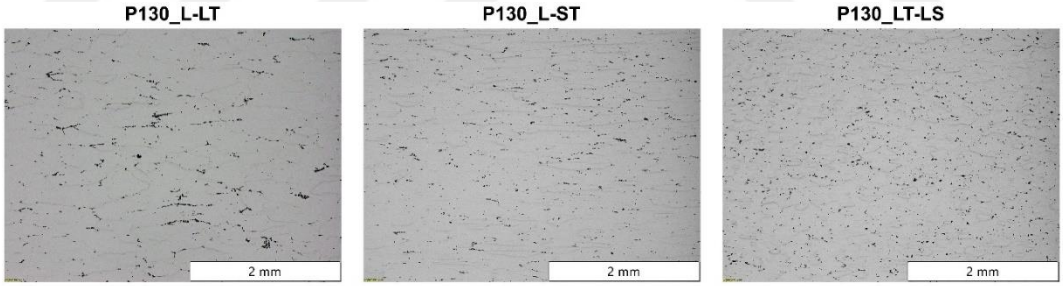

Figure 3.6. Optical microscopy images of the as-polished surfaces of the 130 mm thick plate obtained from three directions.

Table 3.4 Area percentage of second-phase particles on different planes of the 20 and 130 mm plates.

Plate	Plane	Area Percent [%]
P20	L-LT	0.40
	L-ST	0.46
	LT-ST	0.23
P130	L-LT	0.64
	L-ST	0.61
	LT-ST	0.34

The second phase particles in the microstructure of AA2050 T84 were investigated using SEM. The SEM images of the second phase particles in the 20 mm and 130 mm thick plates were examined using the backscattered electrons (BSE) and secondary electrons (SE) detector, and the images are given in Figure 3.7 and Figure 3.8, respectively. Also, EDS analysis and EDS elemental mapping of these particles were carried out to assess their chemical compositions as shown in Figure 3.9 and Figure 3.10-Figure 3.11, respectively. Based on the findings of the EDS analysis, it was determined that AA2050 contains second phase particles compounds composed of Al, Cu, Fe, and Mn.

According to EDS analysis, the second phase particles present in AA2050 can be categorized into two groups: Fe-containing and Mn-containing. It was observed that the Fe-containing particles appear significantly larger than Mn-containing ones. Both particles were observed in the form of clusters. Fe-containing particles were cracked perpendicular to the rolling direction. On the other hand, Mn-containing particles were aligned along the rolling direction (L).

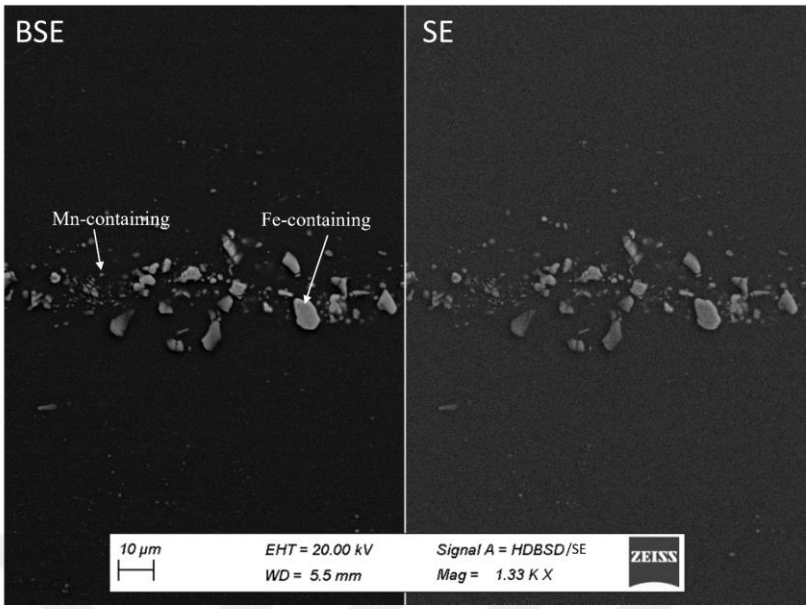

Figure 3.7. Backscattered and secondary electron SEM images of the second phase particles of AA2050-T84 (20 mm thick plate).

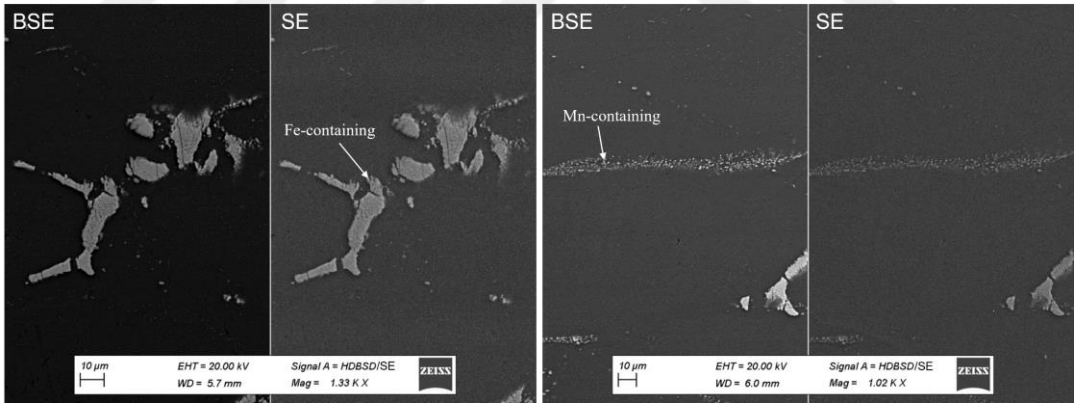

Figure 3.8. Backscattered and secondary electron SEM images of the second phase particles of AA2050-T84 (130 mm thick plate).

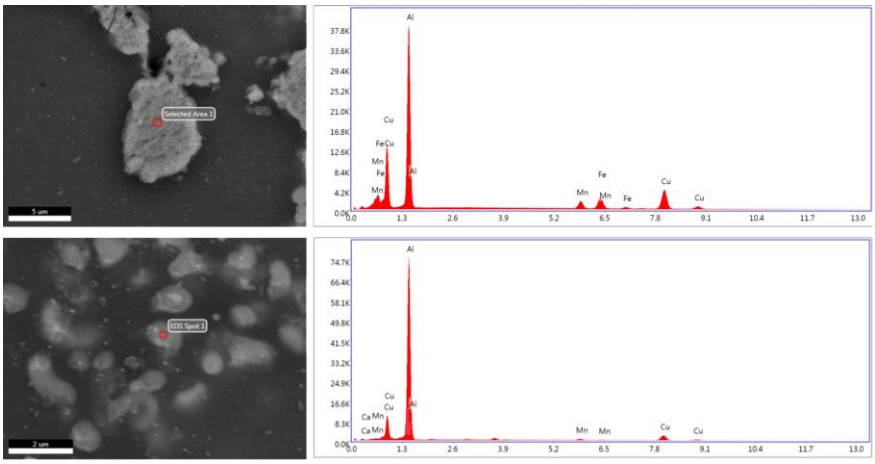

Element	Weight %
Al	50.19
Mn	5.96
Fe	10.50
Cu	33.36

Element	Weight %
Al	80.73
Mn	1.84
Cu	17.43

Figure 3.9. Backscattered SEM images and the corresponding EDS results of the second phase particles.

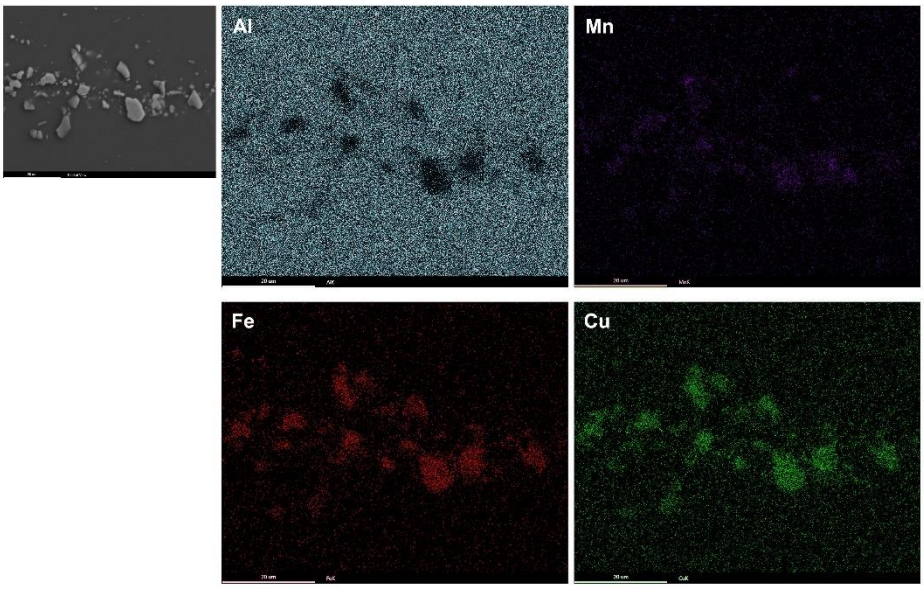

Figure 3.10. EDS elemental mapping of the second phase particles in the 20 mm thick plate.

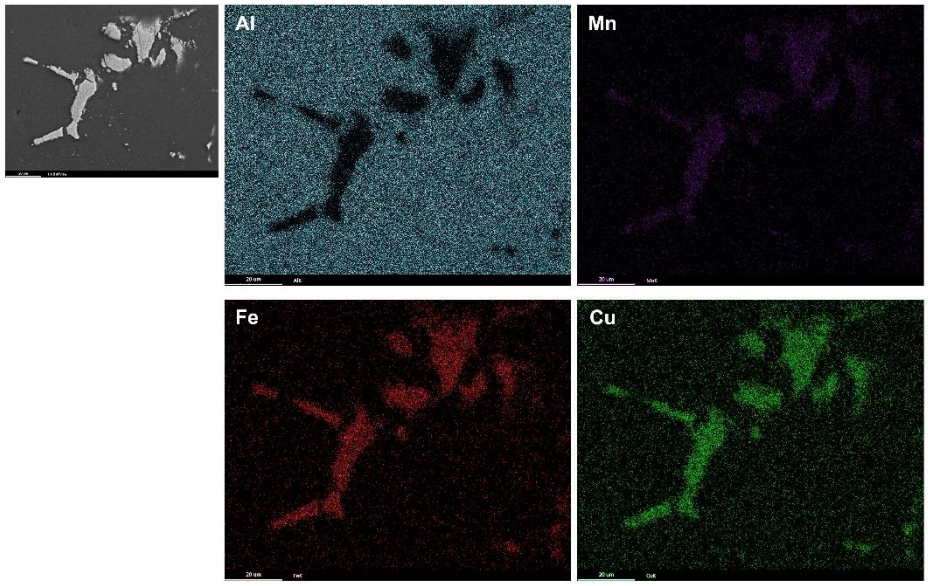

Figure 3.11. EDS elemental mapping of the second phase particles in the 130 mm thick plate.

3.3 XRD Analysis

Normalized XRD patterns obtained from L-LT, L-ST, and LT-ST planes of 20 and 130-mm thick plates are shown in Figure 3.12. All the patterns belong to FCC aluminum. An evident orientation was noted in P20_L-LT and P20_LT-ST, showing a preference towards (200) and (220) planes. Also, compared to the other samples, a relatively increased intensity of (111) planes was observed on the L-ST plane. These findings indicated an evolution of texture in the 20 mm thick plate. This orientation difference was not observed in P130 samples.

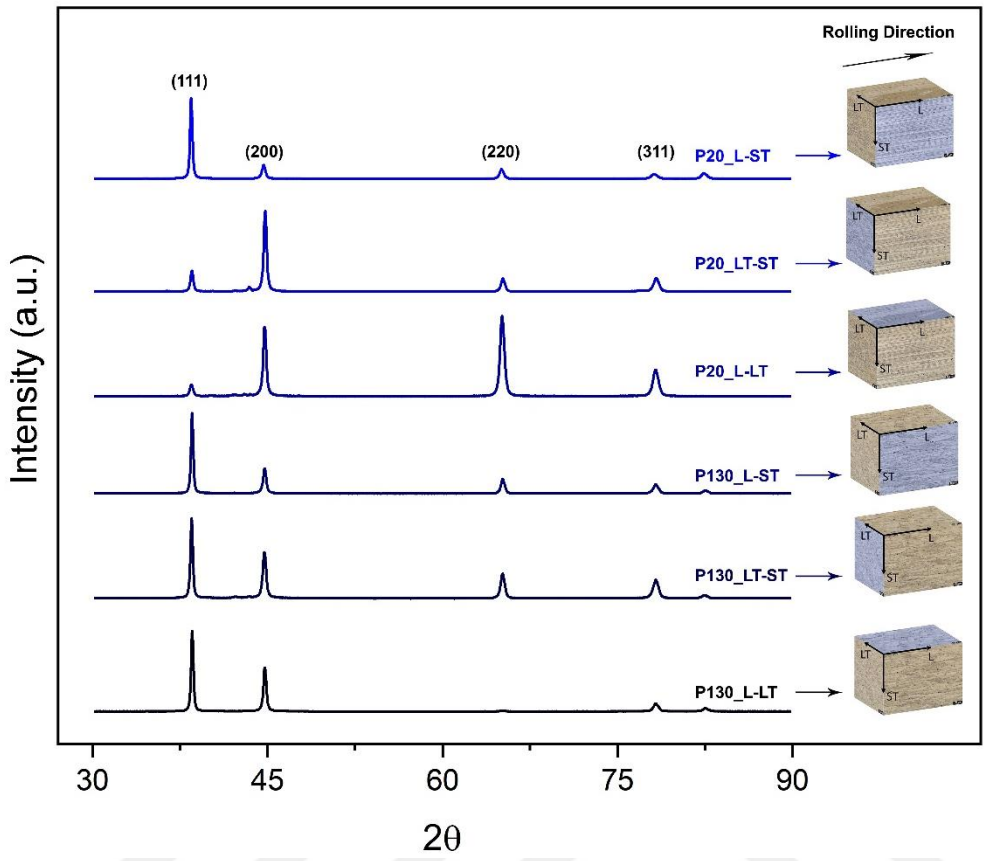

Figure 3.12. Normalized XRD patterns of the L-LT, L-ST, and LT-ST planes of 20 and 130 mm thick plates.

3.4 Hardness Test

Hardness test results of the 5 different indentations used for three directions are shown in the Figure 3.13. Average hardness values are reported in the Table 3.5. Hardness values were measured to be similar in all three directions as expected on both plates. The average hardness value of the 20 mm thick plate was found to be slightly higher than the 130 mm thick plate. This result was attributed to the rolling process applied to the 20 mm thick plate that caused a higher amount of reduction in thickness compared to the 130 mm thick plate [34].

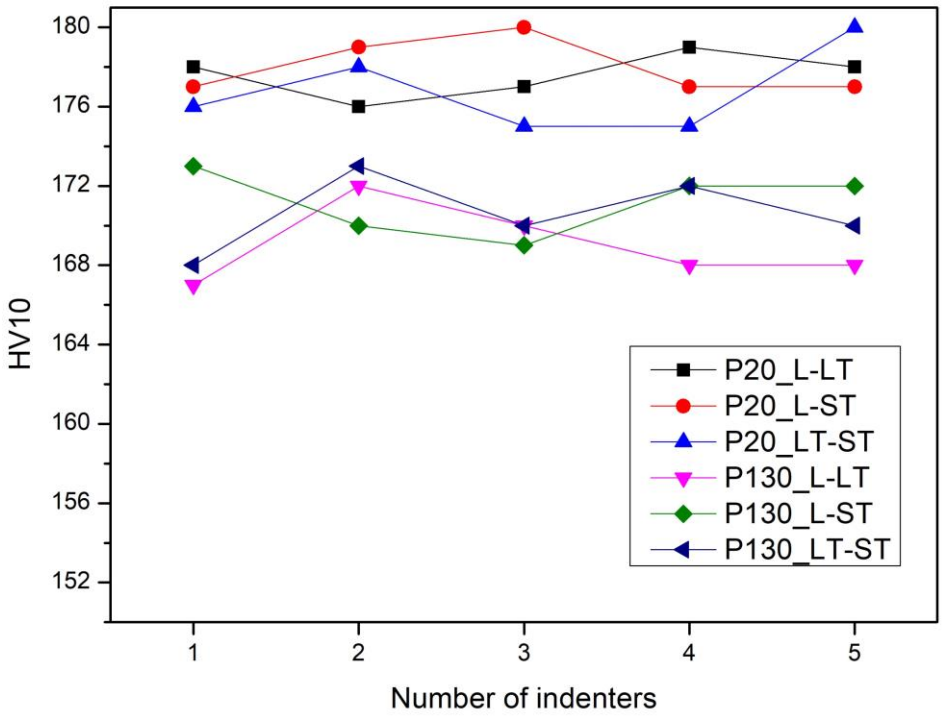

Figure 3.13. Hardness results of the 20 and 130 mm thick plates measured using HV10 method.

Table 3.5 Mean hardness values of 20 and 130 mm thick plates.

Plate	P20	P130
Plane	Mean Hardness Value (HV10)	
L-LT	177.6 ± 1.14	169.0 ± 2.00
L-ST	178.0 ± 1.41	171.2 ± 1.64
LT-ST	176.8 ± 2.17	170,6 ± 1.95

3.5 Tensile Test Results

The tensile test results were used to determine the tensile strength, yield strength, elasticity modulus, and percent elongation values of the samples. These values were obtained from the samples extracted from three different directions (L, LT and 45 degree) of 20 mm thick plate and two different directions (L and LT) of a 130 mm thick plate. It is important to note that not all fractures in the samples occurred inside the extensometer blades.

Stress-strain curves of the 20 mm thick plate from the central location (t/2) in L direction, is presented in Figure 3.14. The average tensile strength of the L-oriented samples was 544 MPa, the average yield strength was 516 MPa, the average elongation at break was 15% and the modulus of elasticity was 76 GPa. These results are reported in Table 3.6.

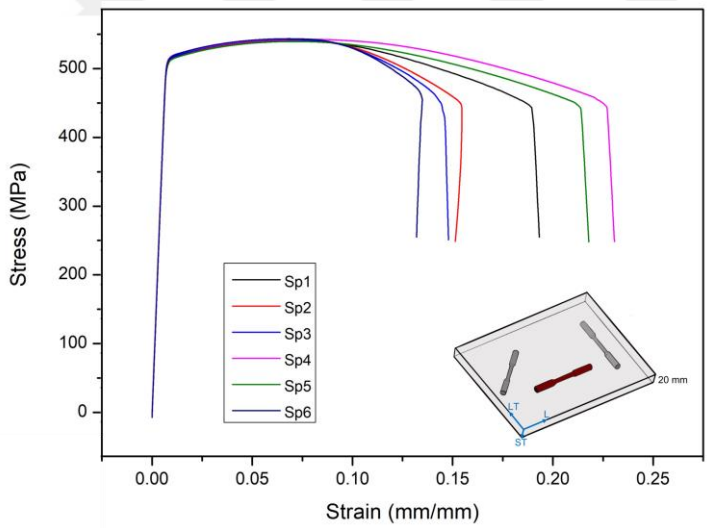

Figure 3.14. The stress-strain plots of the L-oriented samples extracted from the 20 mm thick plate.

Table 3.6 Tensile test results of L-oriented samples extracted from the 20 mm thick plate.

Specimen	Tensile Strength (MPa)	0.2 % Yield Strength (MPa)	Elastic Modulus (GPa)	Elongation (L_0=4D) [%]
SP1	543	514	77	16
SP2	543	516	76	13
SP3	544	516	77	13
SP4	545	519	76	15
SP5	542	514	75	17
SP6	546	518	76	16
Average	544	516	76	15
S. dev.	2	2	1	2

Figure 3.15 shows the stress-strain curve obtained from the samples extracted from the 20 mm thick plate in LT direction. The results for the LT-oriented samples are summarized in Table 3.7, with an average tensile strength of 547 MPa, an average yield strength of 502 MPa, an average elongation at break of 10%, and a modulus of elasticity of 78 GPa.

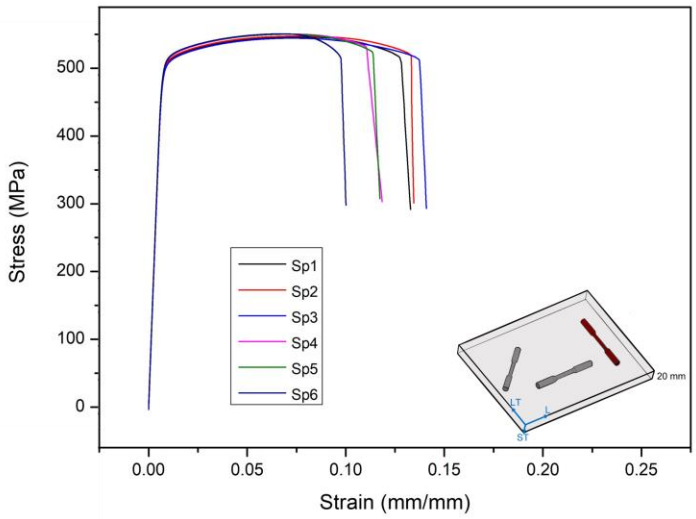

Figure 3.15. The stress-strain plots of the LT-oriented samples extracted from the 20 mm thick plate.

Table 3.7 Tensile test results of LT-oriented samples extracted from the 20 mm thick plate.

Specimen	Tensile Strength (MPa)	0.2 % Yield Strength (MPa)	Elastic Modulus (GPa)	Elongation (L_0=4D) [%]
SP1	545	499	77	7
SP2	546	501	78	13
SP3	543	498	77	11
SP4	549	504	78	11
SP5	549	506	79	9
SP6	549	505	78	11
Average	547	502	78	10
S. dev.	3	3	1	2

In addition to the L and LT directions of 20 mm thick plate, samples in 45-degree direction were also extracted and tested. The results are shown in Figure 3.16. Also, Table 3.8 provides a summary of the results, revealing an average tensile strength of 498 MPa, an average yield strength of 455 MPa, an average elongation at break of 14%, and a modulus of elasticity of 75 GPa. These samples exhibited the lowest tensile and yield strength values among all samples.

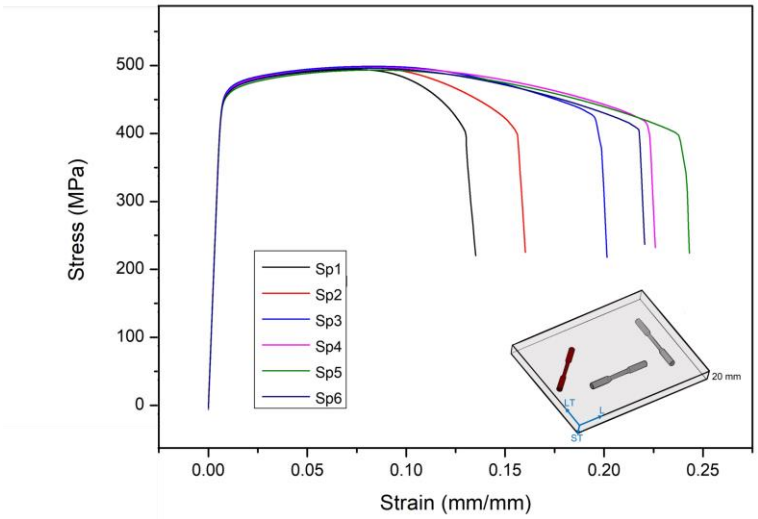

Figure 3.16. The stress-strain plots of the samples extracted in 45^o direction from the 20 mm thick plate.

Table 3.8 Tensile test results of samples extracted in 45^{o} direction from the 20 mm thick plate.

Specimen	Tensile Strength (MPa)	0.2 % Yield Strength (MPa)	Elastic Modulus (GPa)	Elongation (L_0=4D) [%]
SP1	496	454	74	13
SP2	499	456	75	13
SP3	501	458	74	14
SP4	499	455	75	15
SP5	496	452	74	17
SP6	498	454	74	14
Average	498	455	75	14
S. dev.	2	2	0	1

Figure 3.17 illustrates the stress-strain curve derived from the 130 mm thick samples extracted from the quarter thickness location (t/4) in L direction. The average tensile strength of the L-oriented samples was 504 MPa, the average yield strength was 474 MPa, the average elongation at break was 12% and the modulus of elasticity was 75 GPa. These results are reported in Table 3.9.

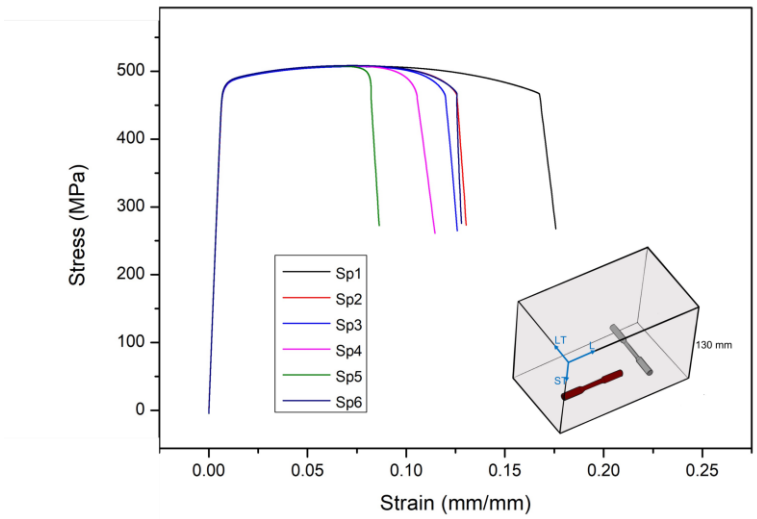

Figure 3.17. The stress-strain plots of the L-oriented samples extracted from the 130 mm thick plate.

Table 3.9 Tensile test results of L-oriented samples extracted from the 130 mm thick plate.

Specimen	Tensile Strength (MPa)	0.2 % Yield Strength (MPa)	Elastic Modulus (GPa)	Elongation (L_0=4D) [%]
SP1	504	474	76	13
SP2	504	474	75	11
SP3	503	473	75	14
SP4	504	475	76	14
SP5	504	475	76	11
SP6	504	475	76	11
Average	504	474	75	12
S. dev.	1	1	1	1

Figure 3.18 shows the stress-strain curve obtained from the samples from the quarter thickness location (t/4) in LT direction. The corresponding results for the LT-oriented samples are summarized in Table 3.10, with an average tensile strength of 514 MPa, an average yield strength of 459 MPa, an average elongation at break of 8%, and a modulus of elasticity of 77 GPa.

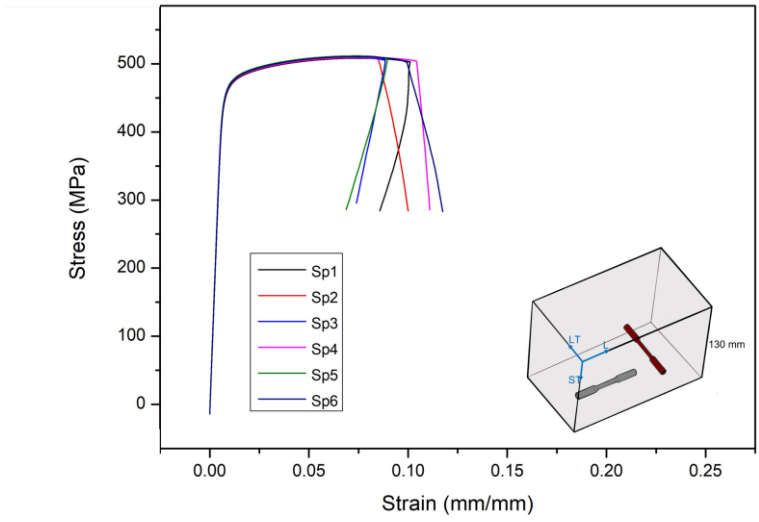

Figure 3.18. The stress-strain plots of the LT-oriented samples extracted from the 130 mm thick plate.

Table 3.10 Tensile test results of LT-oriented samples extracted from the 130 mm thick plate.

Specimen	Tensile Strength (MPa)	0.2 % Yield Strength (MPa)	Elastic Modulus (GPa)	Elongation (L_0=4D) [%]
SP1	513	457	77	8
SP2	513	458	77	8
SP3	513	460	78	7
SP4	514	459	78	9
SP5	516	462	77	9
SP6	515	459	78	9
Average	514	459	77	8
S. dev.	1	2	1	1

Tensile test results showed that both 20 mm and 130 mm thick plates have anisotropic tensile strength, yield strength and % elongation values (elastic modulus values of all samples were similar). The results are compared in Figure 3.19. For instance, the yield strength values of both plates were higher when the tensile tests were performed in the L-direction compared to the LT-direction. The main reason of this result was the grain orientations of the samples. Both plates have oriented grains in the rolling (L) direction. When the stress is applied in the rolling direction, dislocation movement is expected to become perpendicular to the oriented grains/grain boundaries in the L-ST plane. Therefore, the movement of dislocations is expected to be hindered by the elongated grain boundaries. However, the amount of grain boundary region perpendicular to the dislocation movement is lower when the applied stress is in the LT direction, which eases the dislocation movement along the adjacent grains. As expected, the tensile strength of the 130 mm thick plate was higher in the LT-direction (which has a lower yield strength). However, this result was not observed for 20 mm thick plate, in which the tensile strength values of L and LT-directions were similar. This finding was attributed to the texture present in the LT-ST plane (refer to Figure 3.12) on which the dislocation motion and the crack growth is expected to be observed under tensile loading in the L-direction. It should

also be noted that the % elongation values of all samples were in line with their tensile strength values.

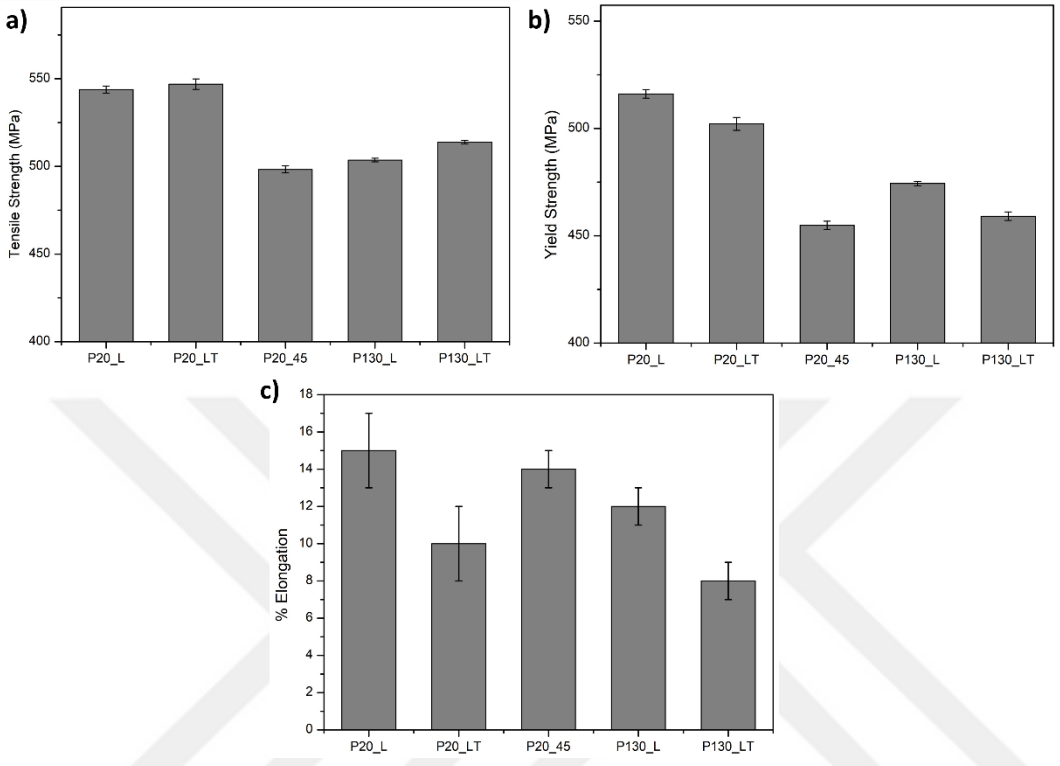

Figure 3.19. Comparison of a) the tensile, b) yield strength results, and c) % elongation values of the samples extracted from 20 and 130 mm thick plates in different orientations.

The after-test photograph of one representative sample from each test set are given in Figure 3.20. In the samples obtained from the L direction of 20 mm and 130 mm thick plates, cup and cone fracture was observed, whereas this type of fracture was not observed in the samples extracted from the LT direction. In fact, the failure mode was shear fracture in the LT directions of both sample groups.

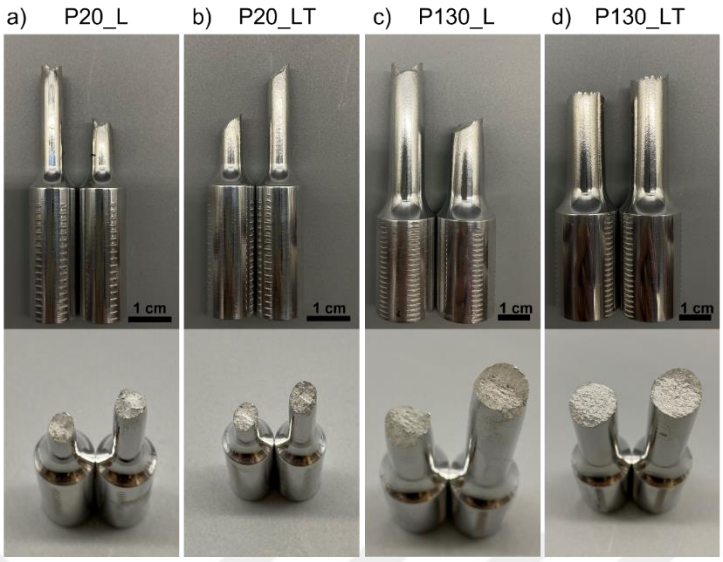

Figure 3.20. After-tensile-test photographs of a) P20-L, b) P20-LT, c) P130- L, and d) P130- LT.

Figure 3.21 and Figure 3.22 show SEM images of the fracture surfaces of P20 and P30 test specimens, respectively. As expected, transgranular ductile fracture (dimpled structure) was observed on all fracture surfaces. The elongated grain morphologies in the L direction are clearly visible on the fracture surfaces of both P20_LT and P130_LT samples.

In the dimples, rod-like and round-like particles were observed at high magnifications as shown in Figure 3.23. The particles are thought to be Manganese (Mn) and zirconium (Zr) based dispersoids present in Al-Cu-Li alloys [1]. It was reported in literature that Mn and Zr play a crucial role in facilitating the formation of an unrecrystallized structure by precipitating as dispersoids. They are reported to form in a homogeneous manner and hinder the recrystallization of grains by grain boundary pinning. The size and distribution of these dispersoids are known to determine the size of the dimples in aluminum alloys [35]. SEM images showing the fracture surfaces of the samples exhibited that the dimple size on the fracture surface of all samples were similar. This result was an indication of well-distributed dispersoids in all samples.

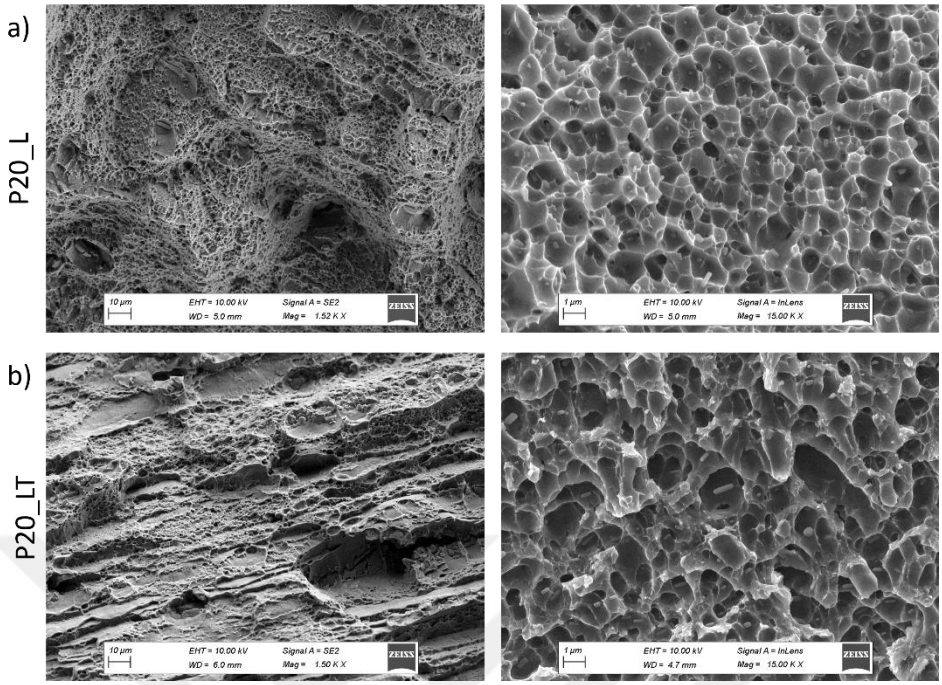

Figure 3.21. Low and high magnification SEM images of the fracture surface of a) P20_L and b) P20_LT after the tensile test.

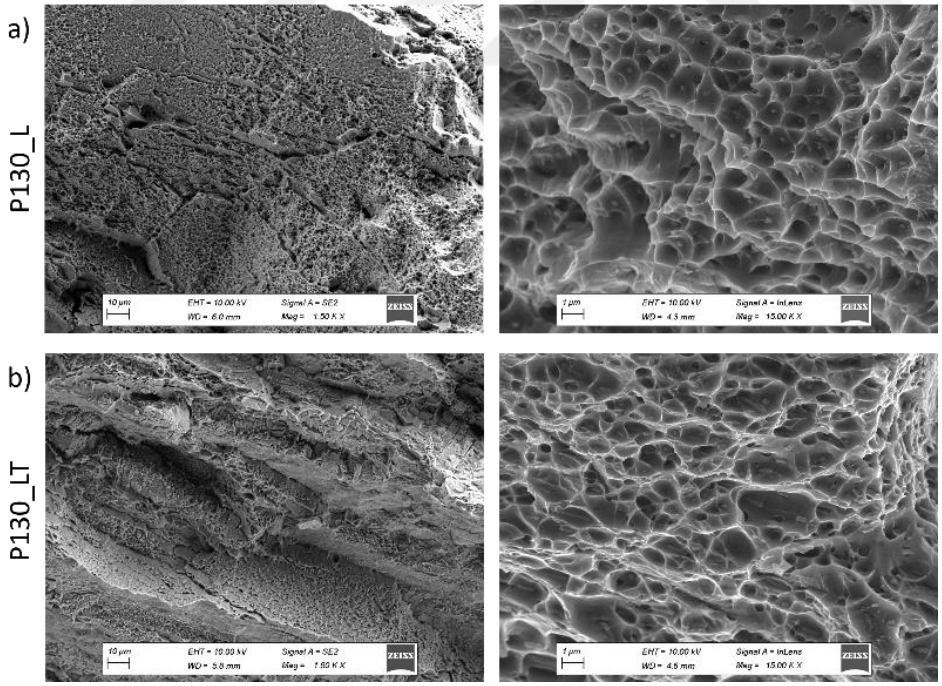

Figure 3.22. Low and high magnification SEM images of the fracture surface of a) P130_L and b) P130_LT after the tensile test.

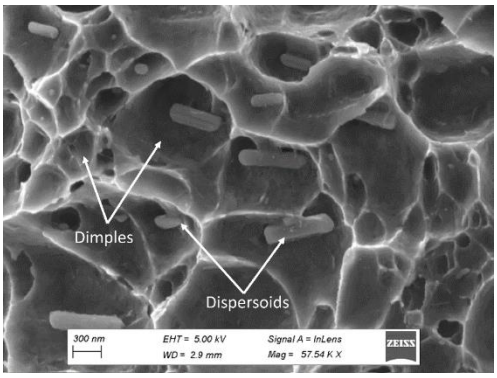

Figure 3.23. SEM image showing the dispersoids in the dimples.

3.6 Impact Test

The P_20LT and P20_L samples have the impact energies of 9 J and 67 J, respectively. The impact energies of the P130_LT and P130_L samples were 5 J and 10 J, respectively. P130_L sample has higher impact energy compared to other specimens. After-test photographs of test specimens were given in Figure 3.24. The results revealed distinct fracture surface characteristics between the two sample groups. Specifically, the samples extracted from the transverse direction exhibited a flat fracture surface, whereas the samples obtained from the rolling direction displayed irregularly fractured surfaces.

Impact test results showed that the impact energies of the L-oriented specimens were higher than the LT-oriented specimens, for both 20 mm and 130 mm thick plates. These results could be correlated with the anisotropic grain structure of the plates. In both plates, the grains are oriented in the rolling direction. Therefore, for the L-oriented specimens, dislocation motion and crack growth are expected to take place perpendicular to the grain boundaries. This required more energy for the crack growth as the cracks propagate through the grains. On the other hand, for LT-oriented specimens, crack growth is expected to take place along the grain boundaries, which eases the crack propagation and decreases the impact energy. It is important to note that L-oriented sample extracted from the 20 mm thick plate had a

significantly higher impact energy than the other samples. Highly irregular fracture surface having deep secondary cracks was also observed for this sample. This behavior was attributed to two main reasons. First, 20 mm thick plate has grains with a very high aspect ratio (27) in the rolling direction. Therefore, it was reasonable to expect that highly oriented parallel grain boundaries acted as obstacles for the propagating crack and required comparatively high energy. As a result, deep secondary cracks formed parallel to the rolling direction. Also, XRD results showed that LT-ST plane is a textured surface at which crack propagates for L-direction samples. This plane has a higher density of (002) and (022) planes than (111) plane where the first two requires higher energy for the crack propagation. Collectively, the high-aspect-ratio grains in the rolling direction together with the textured surface, P20_L sample has the highest impact energy among all samples.

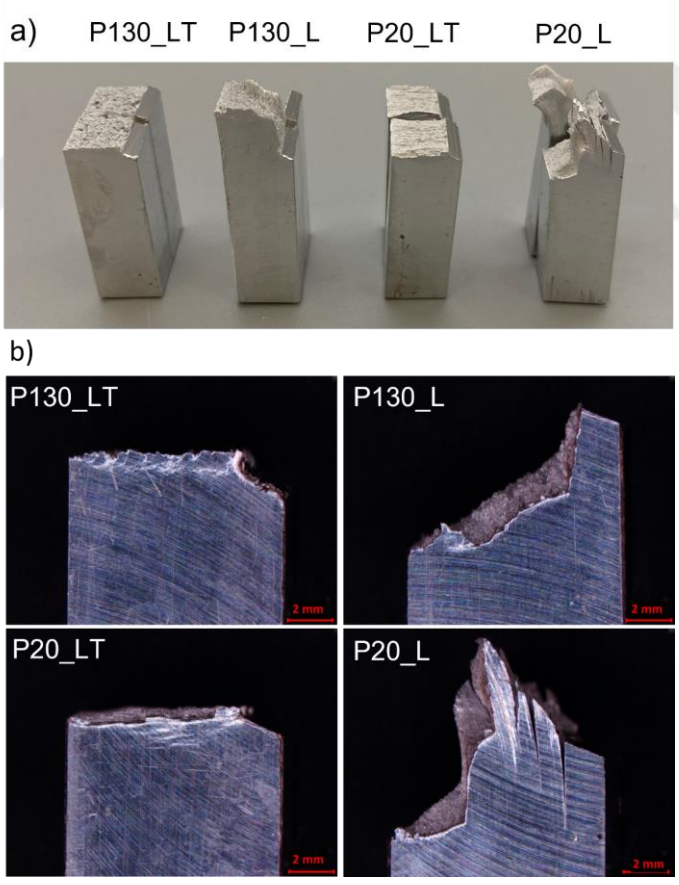

Figure 3.24. a) Photographs and b) Stereomicroscope images of the test specimens after the Charpy impact test.

The fracture surfaces of P20 and P130 test samples were investigated under SEM. SEM images of the specimens were given in Figure 3.25. Grain facets were observed on the fracture surface of all samples. Also, equiaxed ductile dimples were present on the facet surfaces for each sample on the crack initiation and propagation regions. The size and morphology of the facets observed on the fracture surface of the samples matched with their grain size and morphology. Therefore, the presence of the facets could be originated from the precipitate free zones (PFZ) at the near grain boundary regions of the samples [25]. However, on the final fracture zones only dimpled structure was observed for each sample, characteristic to FCC aluminum alloys.

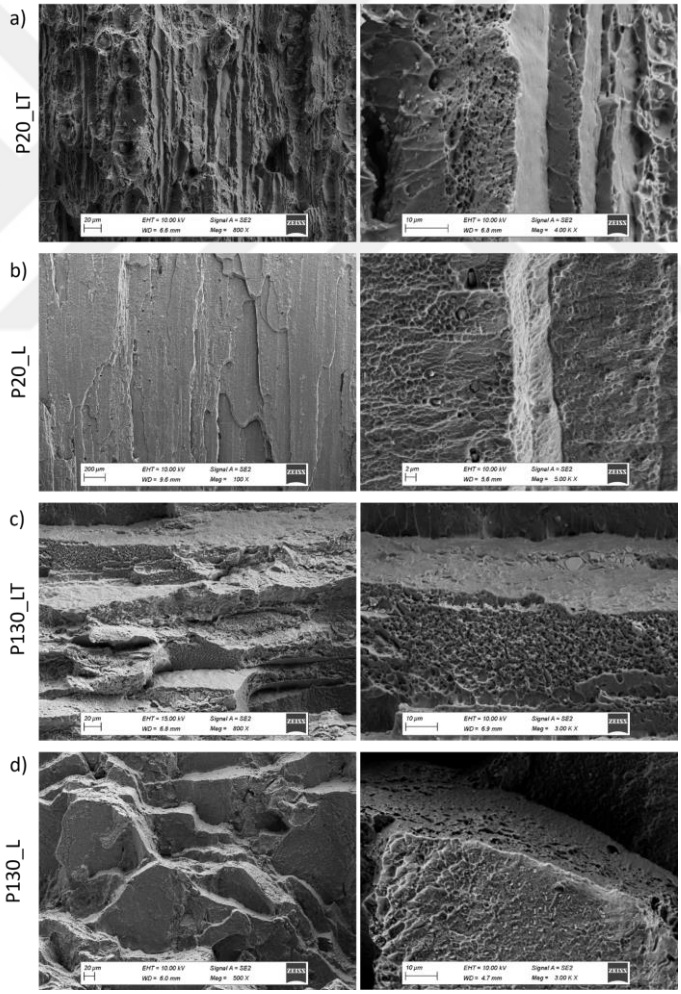

Figure 3.25. Low and high magnification SEM images of a) P20_LT, b) P20_L c) P130_LT, and d) P130_L after the Charpy impact test.

3.7 High Cycle Fatigue Test Result

The fatigue characteristics of 20 mm and 130 mm thick plates were investigated using specimens having L and T directions. The S-N curves of P20 and P130 samples were provided in Figure 3.26 and Figure 3.27, respectively.

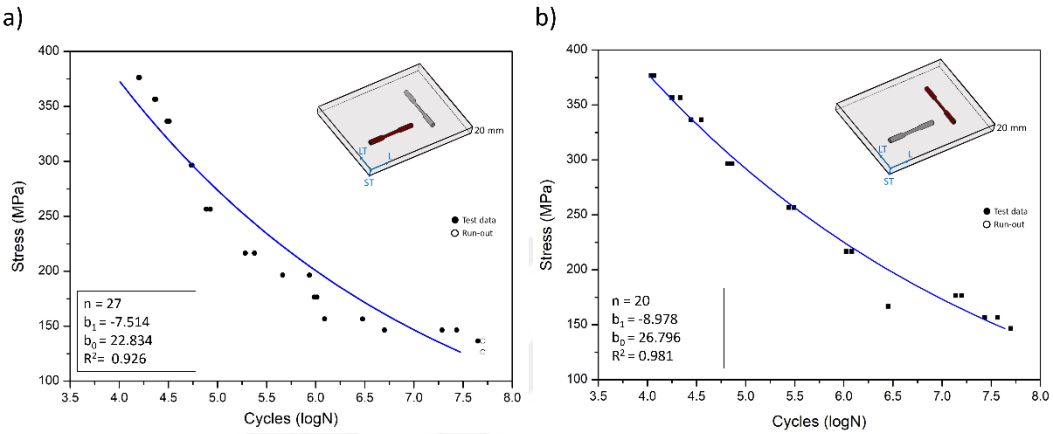

Figure 3.26. S-N Curves of a) P20_L and b) P20_LT.

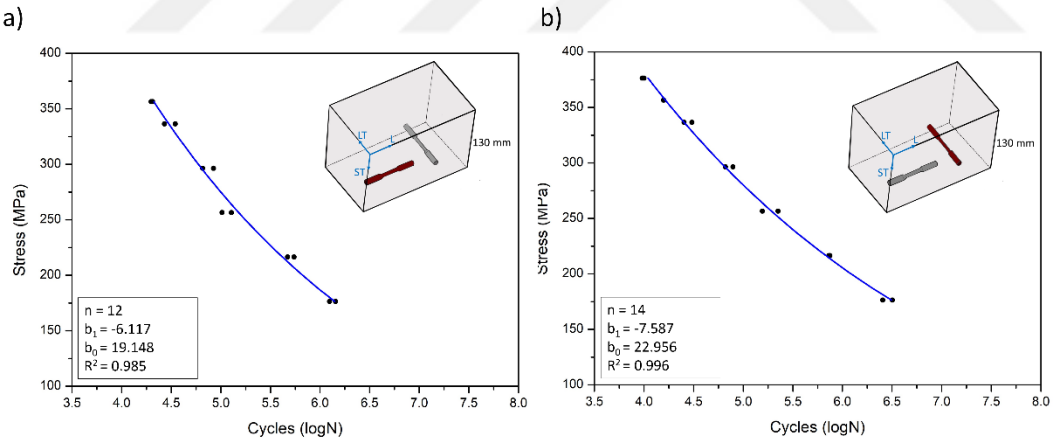

Figure 3.27. S-N Curves of a) P130_L and b) P130_LT.

S-N curves of all sample groups are compared in Figure 3.28. LT-oriented specimens exhibited higher fatigue life in both the 20 mm and 130 mm thick plates. This observation was attributed to the inherent lower strength values observed in the L direction when compared to the LT direction for both plate thicknesses. Additionally,

it was observed that the fatigue life increased as the stock thickness decreased. This finding is consistent with the tensile test results where 20 mm thick plate has a higher strength value than the 130 mm thick plate.

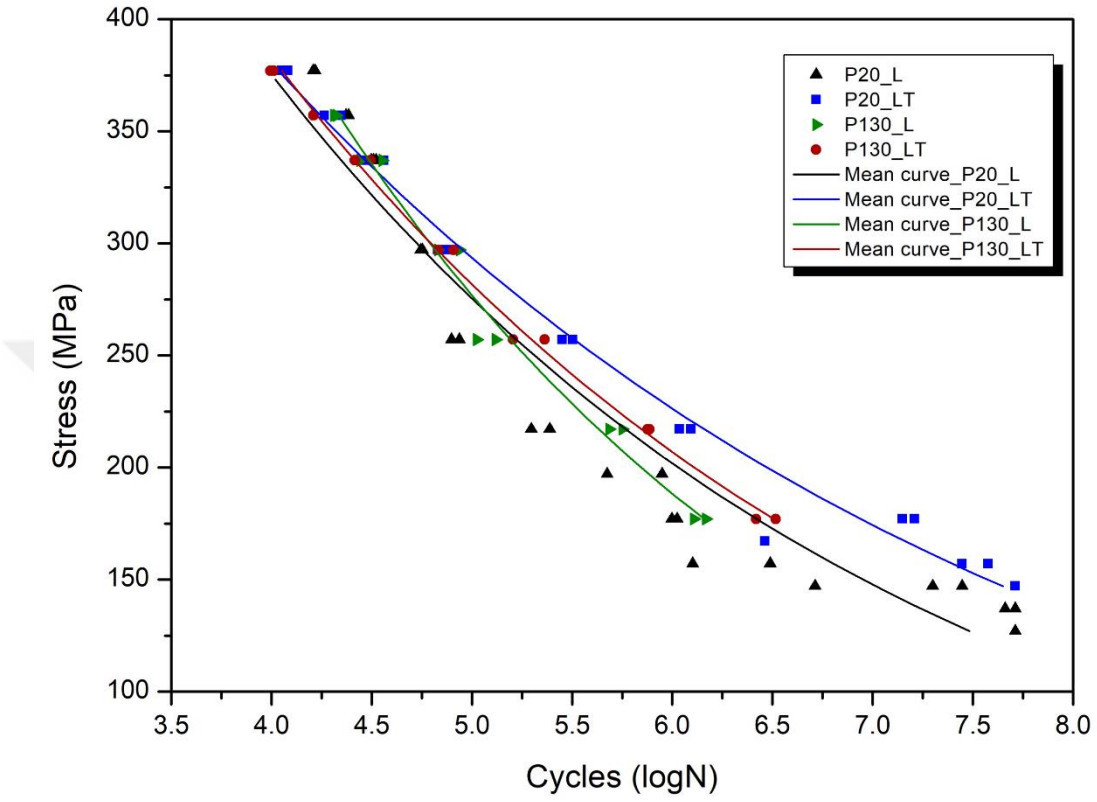

Figure 3.28. Comparison of the S-N curves of all sample groups.

SEM images of the fracture surfaces of representative samples from each test group subjected to identical low stress levels are shown in Figure 3.29 and Figure 3.30 for 20 mm and 130 mm thick plates. Crack initiation mechanism was crystallographic slip for all specimens. Notably, in the LT-oriented sample extracted from the 20 mm thick plate, sub-surface fatigue crack initiation (2 mm beneath the surface) was observed, while in the L-oriented sample, the crack initiation occurred at the surface. For the L and LT-oriented specimens obtained from the 130 mm thick plate, sub-surface fatigue crack initiation was identified, with the crack initiation sites approximately 1.5 mm and 200 μm beneath the surface, respectively.

Further analysis revealed that the stage I region in the LT samples was significantly larger than in the L samples for both the 20 mm and 130 mm thick plate specimens, attributed to elongated grains. This observation agrees that the LT-oriented specimens in both thicknesses exhibit an extended fatigue life, compared to L-oriented specimens.

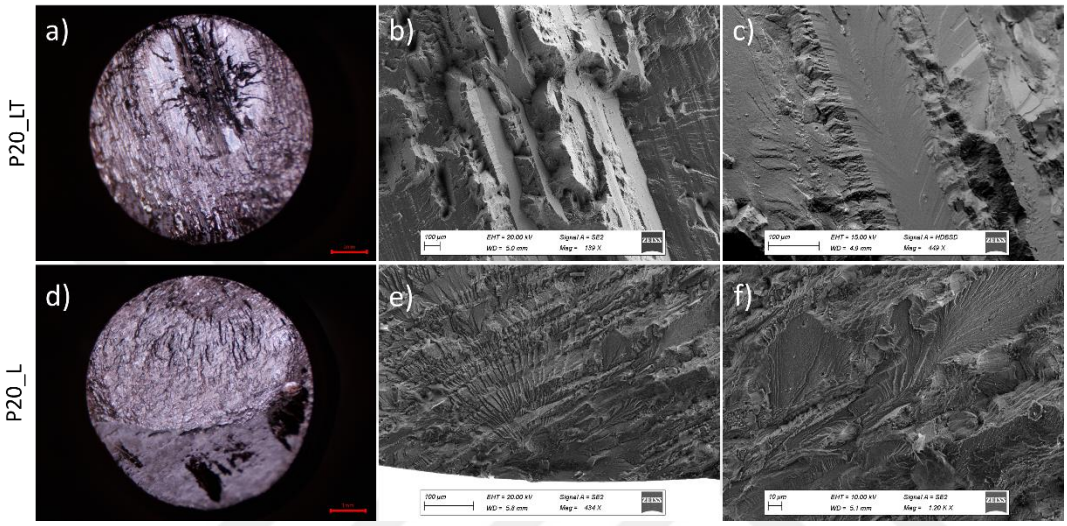

Figure 3.29. a) Stereomicroscope, b) low, and c) high magnification SEM images of the HCF test specimen of P20_LT, and d) stereomicroscope, e) low, and f) high magnification SEM images of the HCF test specimen of P20_L. (SEM images are captured from fatigue crack initiation regions.)

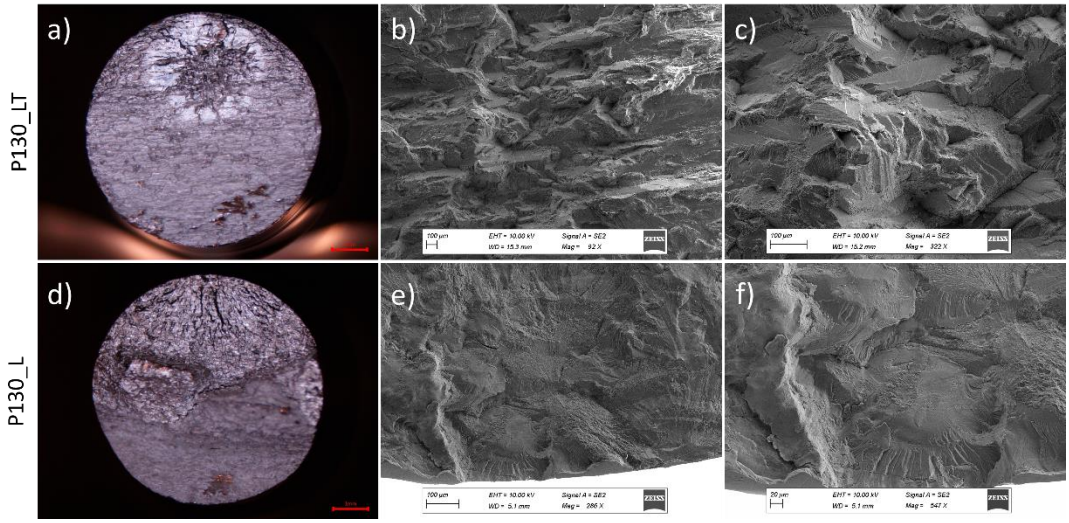

Figure 3.30. a) Stereomicroscope, b) low, and c) high magnification SEM images of the HCF test specimen of P130_LT, and d) stereomicroscope, e) low, and f) high magnification SEM images of the HCF test specimen of P130_L. (SEM images are captured from fatigue crack initiation regions.)

3.8 Crack Growth Rate Results

Fatigue crack growth tests of L-T and T-L oriented specimens extracted from 20 mm and 130 mm thick plates were performed under a stress ratio of R = 0.1. The samples extracted from the 20 mm thick plate were named as P20_T-L and P20_L-T following their orientations. Three samples (Sp1, Sp2 and Sp3) for the P20_T-L configuration and two samples (Sp4 and Sp5) for the P20_L-T configuration were tested. Likewise, the samples with two different orientations extracted from the 130 mm plate were named as P130_T-L and P130_L-T. Three samples (Sp1, Sp2 and Sp3) for the P130_T-L configuration and two samples (Sp4 and Sp5) for the P130_L-T configuration were tested.

The Crack Opening Displacement (COD) method was used to measure the crack size and calculations were done using the front-face compliance method specified in ASTM E674. Crack length vs. number of cycle (N) plots are compared in Figure 3.31 for L-T and T-L oriented specimens extracted from 20 mm and 130 mm thick plates.

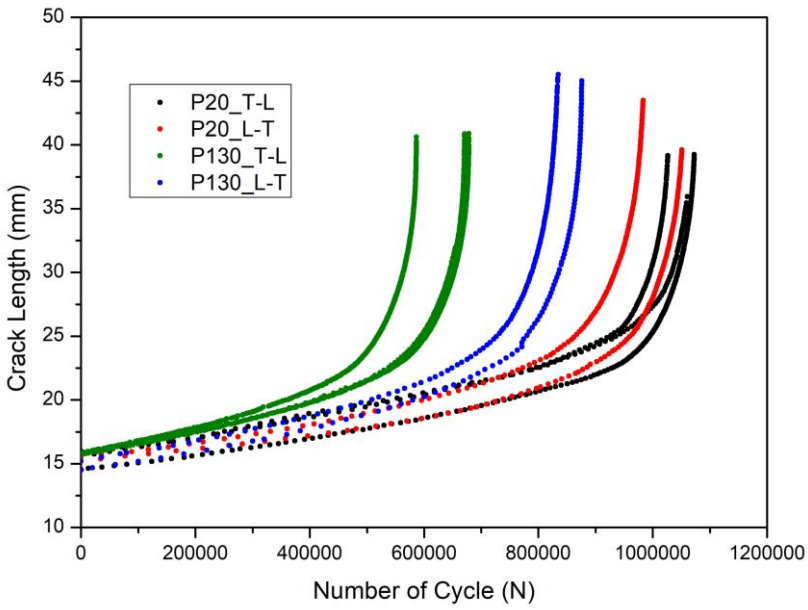

Figure 3.31. Comparison of the crack length vs number of cycle plots of all sample groups.

da/dN – ΔK plots of the P20_T-L and P20_L-T specimens are shown in Figure 3.32 and Figure 3.33, respectively. Also, da/dN – ΔK plots of the P130_T-L and P130_L-T specimens are shown in Figure 3.34 and Figure 3.35, respectively. The crack growth rate calculations were performed using the Incremental Polynomial Method of order 7, as specified in ASTM E647-15. The coefficient "C" and the exponent "m" were determined by plotting the best-fit linear line on the logarithmic scale of (da/dN) versus log ΔK. The experimentally calculated Paris-Erdogan region constants, C and m, are summarized in Table 3.11.

Test results of P20_L-T specimens are invalid since crack deviation was observed on the L-T oriented samples. According to the standard, if a crack deviation occurs with greater than 20^{o} to the normal plane of loading direction for a length of greater than 0.1W, test results would be invalid. In the P20_L-T configuration, the cracks observed in the two tested samples exhibited angular deviations of greater than 20^{o} degrees at a length exceeding 0.1 times the specimen width.

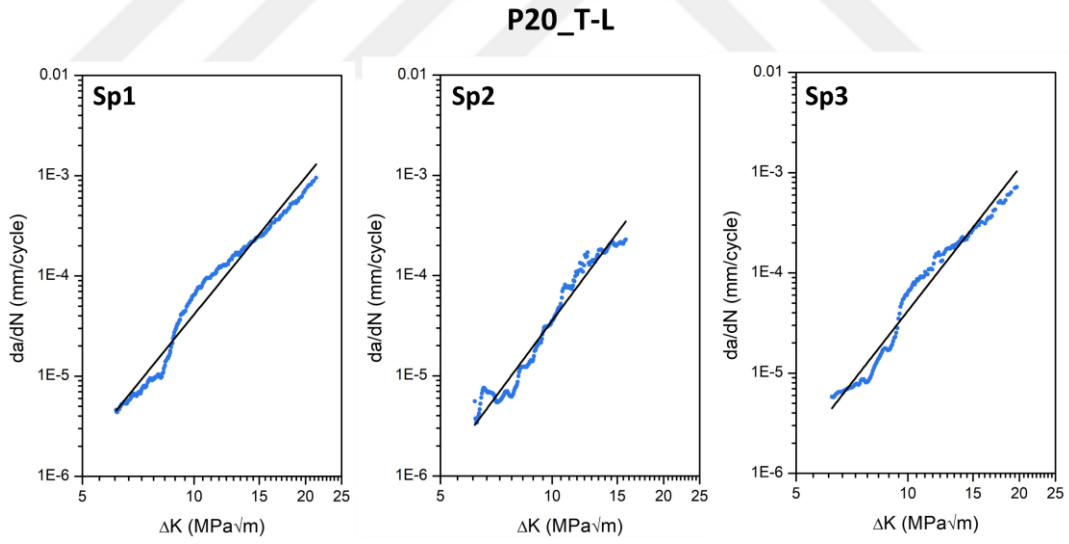

Figure 3.32. da/dN vs ΔK Plots of Sp1, Sp2, and Sp3 extracted from the 20 mm thick plate. Tests were carried out under the stress ratios of 0.1 and the samples were in T-L orientation

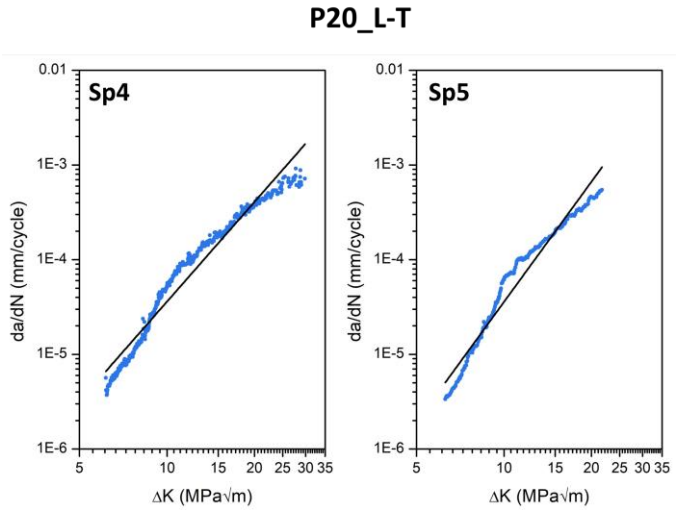

Figure 3.33. da/dN vs ΔK Plots of Sp4 and Sp5 extracted from the 20 mm thick plate. Tests were carried out under the stress ratios of 0.1 and the samples were in L-T orientation. (Test results are invalid due to the crack deviation.)

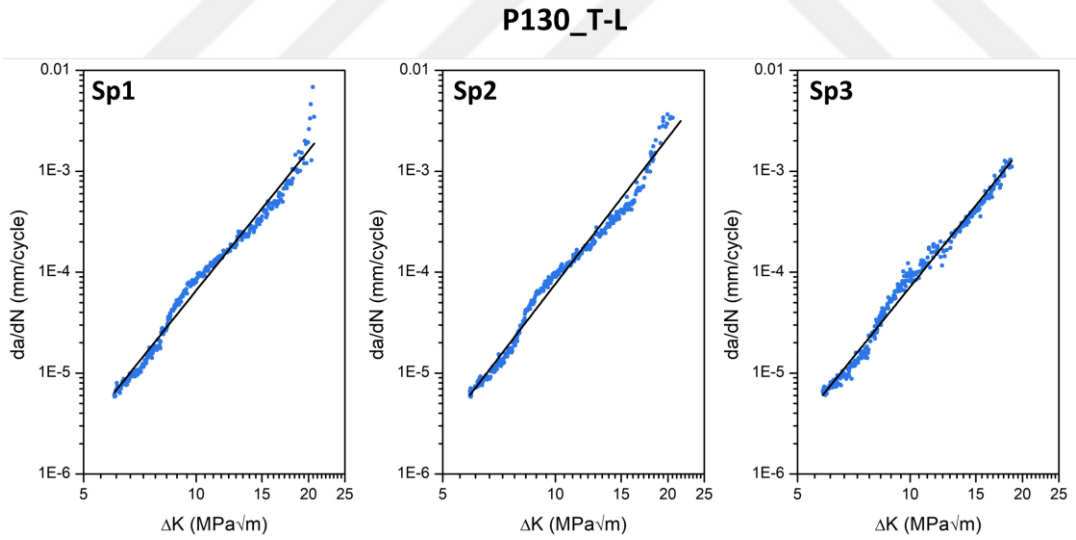

Figure 3.34. da/dN vs ΔK Plots of Sp1, Sp2, and Sp3 extracted from the 130 mm thick plate. Tests were carried out under the stress ratios of 0.1 and the samples were in T-L orientation.

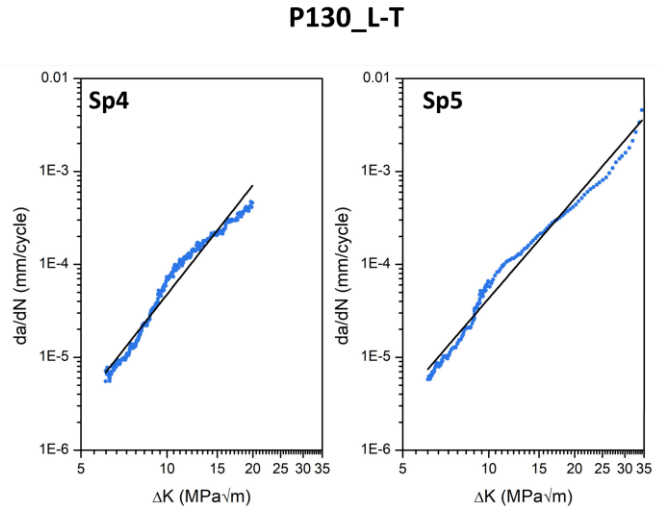

Figure 3.35. da/dN vs ΔK Plots of Sp4 and Sp5 extracted from the 20 mm thick plate. Tests were carried out under the stress ratios of 0.1 and the samples were in L-T orientation.

Table 3.11 Paris-Erdoğan regime constants of specimens.

Specimen	C	m	R^2	$\frac{da}{dN} = C(\Delta K)^m$
P20_ T-L (Sp1)	-8.848	4.537	0.985	$-8.848\ (\Delta K)^{4.537}$
P20_ T-L (Sp2)	-9.250	4.966	0.981	$-9.250\ (\Delta K)^{4.966}$
P20_ T-L (Sp3)	-9.024	4.720	0.983	$-9.024\ (\Delta K)^{4.720}$
P20_ L-T (Sp4)	-7.846	3.482	0.769	$-7.846\ (\Delta K)^{3.482}$
P20_ L-T (Sp5)	-8.506	4.194	0.978	$-8.506\ (\Delta K)^{4.194}$
P130_ T-L (Sp1)	-8.709	4.598	0.991	$-8.709\ (\Delta K)^{4.598}$
P130_ T-L (Sp2)	-8.838	4.792	0.989	$-8.838(\Delta K)^{4.792}$
P130_ T-L (Sp3)	-8.669	4.567	0.994	$-8.669(\Delta K)^{4.567}$
P130_ L-T (Sp4)	-8.158	3.890	0.983	$-8.158(\Delta K)^{3.890}$
P130_ L-T (Sp5)	-7.859	3.553	0.989	$-7.859(\Delta K)^{3.553}$

The after-test photograph of one representative sample from each test set are given in Figure 3.36. There was no deviation in the samples P20_T-L, P130_T-L and P130_L-T. Figure 3.36b illustrates sample P20_L-T with a crack deviating at an angle greater than 20 degrees.

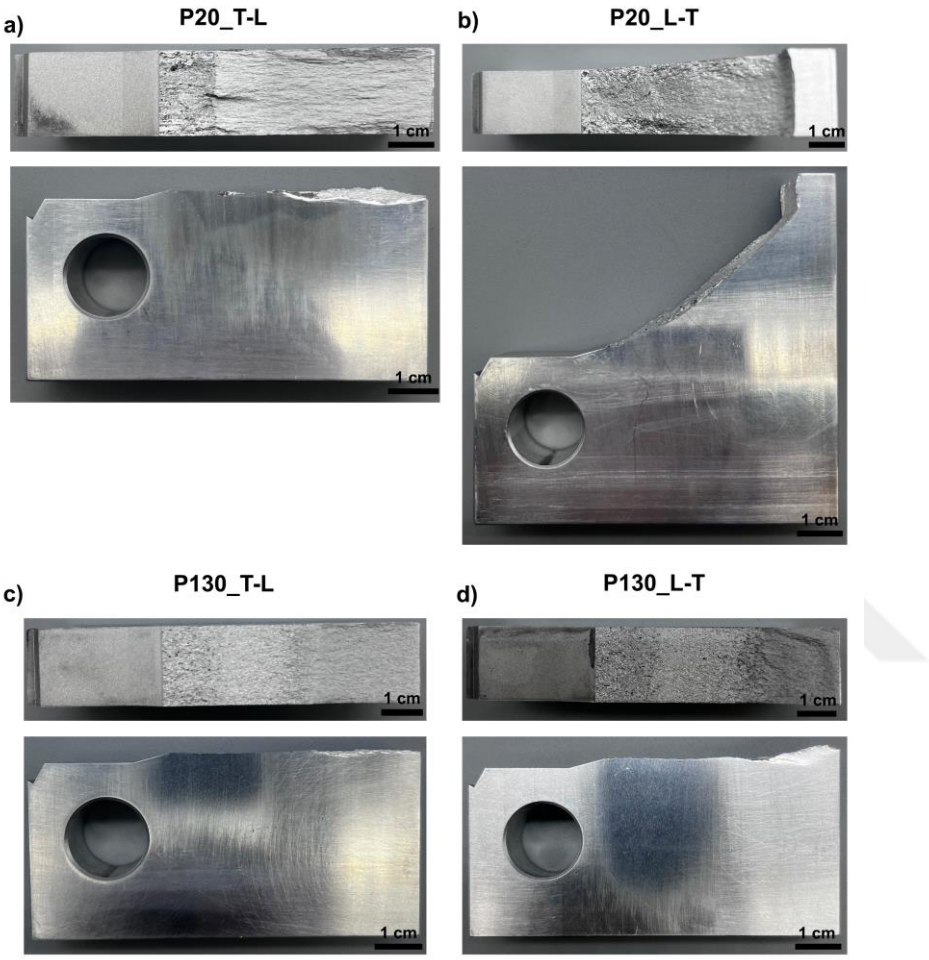

Figure 3.36. Fracture surface and side view photographs after FCG test of one representative sample of a) P20_T-L, b) P20_L-T, c) P130_T-L, and d) P130_L-T.

Comparison of the da/dN-ΔK plots for the P130_T-L, and P130_L-T are shown in Figure 3.37. P130_L-T samples exhibited a slightly lower crack growth rate than the P130_T-L. This orientation-dependent difference in the FCGR was observed to become more prominent at high ΔK due to the larger fracture toughness of the L-T-oriented samples [20]. The elongated grain boundaries perpendicular to the crack

growth direction might be the reason for the slower crack growth rate of the P130_L-T samples, as they acted as barriers for the crack growth, and caused a decrease in fatigue crack growth rate (FCGR). For the 130_T-L samples, the crack growth direction was parallel to the rolling direction, which eliminates the barrier effect of the grain boundaries.

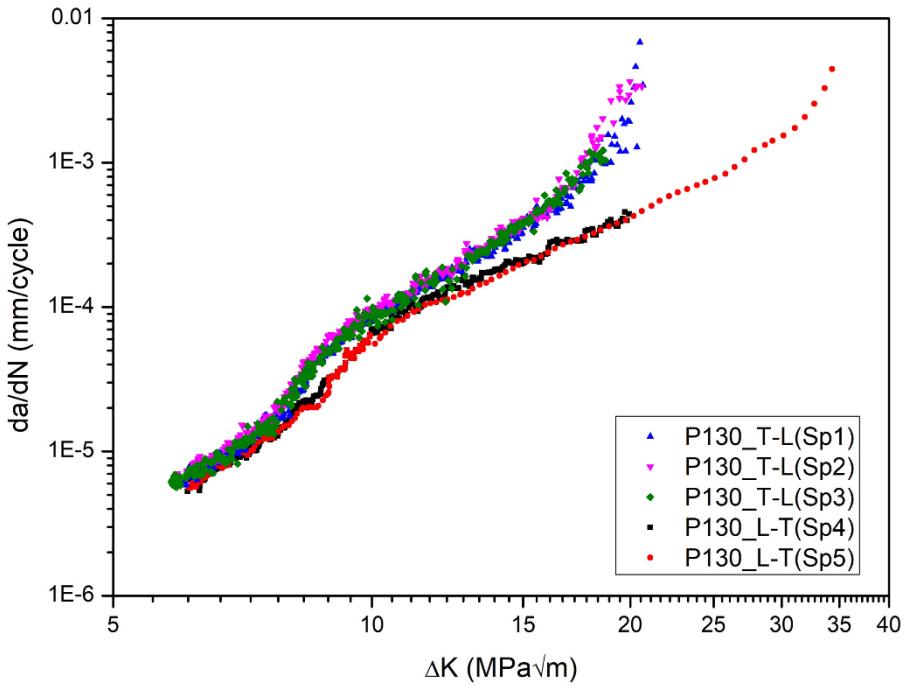

Figure 3.37. da/dN vs ΔK plots of specimens extracted from the 130 mm thick plate in T-L orientation and L-T orientation.

Comparison of the fatigue crack growth curves of the T-L orientation for both P20 and P130 plates are given in Figure 3.38. FCGR of the samples with T-L orientation extracted from the 130 mm thick plate was observed to be slightly higher than that of the 20 mm thick plate. This result can be attributed to the large grains of the 20 mm thick plate with a very high aspect ratio, and the coarse planar slip [36]. Larger grains cause longer distances for dislocation motion to reach the crack tip and contribute to the crack growth. This process requires more energy and slows down the crack growth rate. Planar slip, on the other hand, causes inhomogeneous deformation and favors fracture along slip planes [36]. As a result, crack branching

occurs, causing the formation of a tortuous fracture surface with a slower crack growth rate.

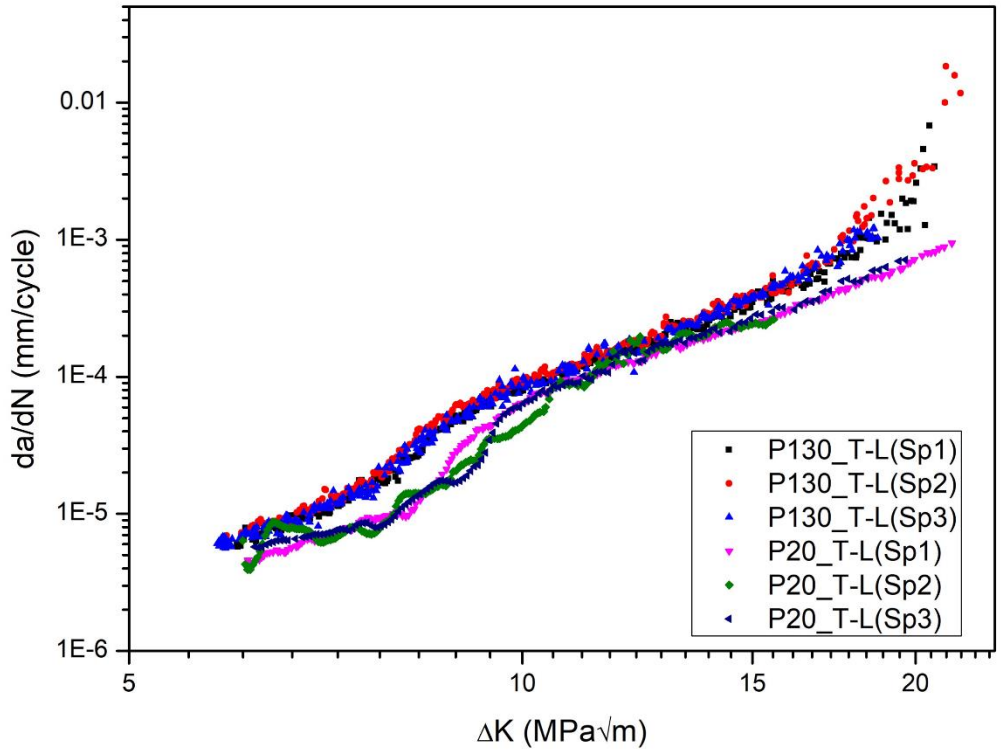

Figure 3.38. da/dN vs ΔK plots of specimens extracted from the 20 mm and 130 mm thick plate in T-L orientation

The crack deviated in the P20_L-T sample at an angle larger than 20^{o} from the expected crack propagation direction, making the test results invalid for this sample group. Still, da/dN vs. ΔK plots of P20_T-L and P20_L-T (invalid) samples are compared in Figure 3.39. Normally, the FCGR of P20_L-T was expected to be slower than the P20_T-L, similar to the 130 mm thick plate samples. However, the crack propagated in a direction close to the lowest tensile and yield strength orientation (45^{o}, as shown in Figure 6) in the P20_L-T sample. Therefore, the real FCGR of the L-T-oriented samples extracted from the 20 mm thick plates could not be measured.

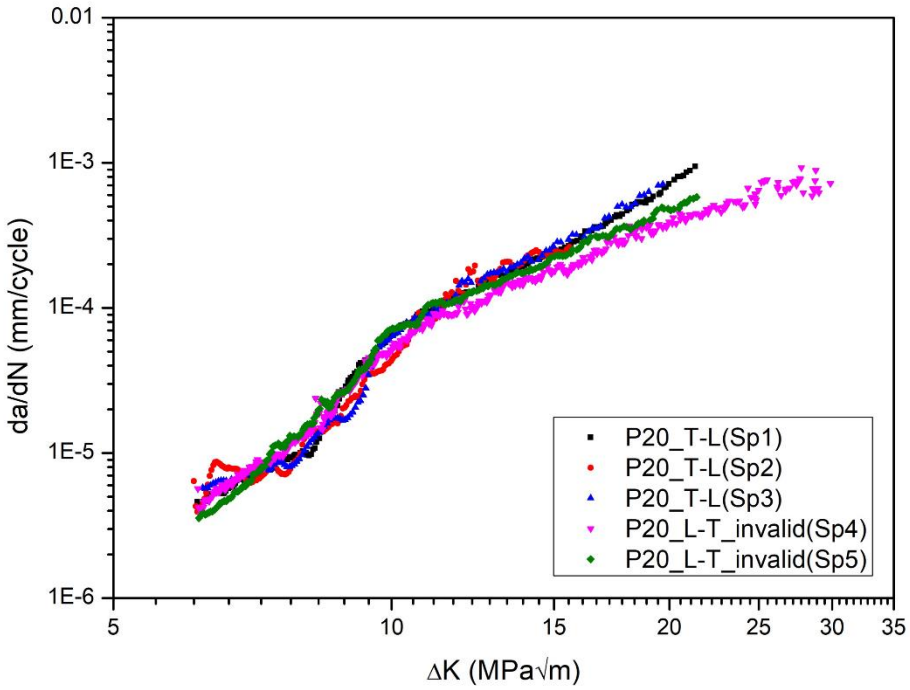

Figure 3.39. da/dN vs ΔK Plots of specimens extracted from the 20 mm thick plate in T-L and L-T orientation.

3.9 Fractographic Analysis of the Fatigue Crack Growth Specimens

One representative sample was selected from each test specimen for the fractographic analyses. Stereo microscope images of the fracture surface morphology of these specimens used in crack propagation tests are shown in Figure 3.40. Cracks propagated macroscopically in pure mode-I direction in P20_T-L, P130_T-L, and P130_L-T samples. However, as it was mentioned in Section 3.8, a noticeable deviation of over 20 degrees from the pure mode-I direction was noticed in the P20_L-T samples. It was observed that the fracture surface of the P20_L-T samples was rougher than P20_T-L samples. No significant surface roughness difference was observed between the fracture surfaces of the P130_L-T and P130_T-L samples. Comparing the fracture surfaces of 20 and 130 mm thick plates, a larger surface roughness was evident for the former than the latter, especially at the stage I

where the crystallographic crack propagation. This difference was attributed to the larger grain dimensions of 20 mm thick plate in the LT direction.

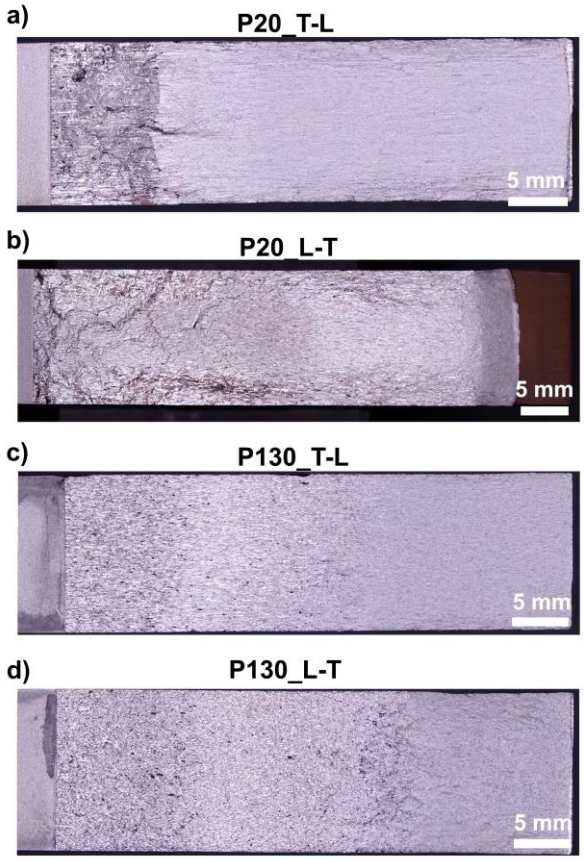

Figure 3.40. Stereomicroscope images of the fracture surface of a) P20_T-L, b) P20_L-T, C) P130_T-L, and d) P130_L-T.

It should be noted that the near-surface regions of 20 mm thick plates exhibited a rougher appearance than their middle regions. This result was also correlated with the grain size of 20 mm thick plates where the grains at the near surface regions were larger than the grains at the middle regions. This difference in the grain size of the 20 mm thick plate is apparent in the whole-thickness CT specimen microstructures captured in two orientations, L-ST and LT-ST, as given in Figure 3.41.

Figure 3.41. Whole-thickness microstructures of 20 mm thick plate CT specimen captured from L-ST and LT-ST planes.

The length of the precrack regions was 3.7 mm for each sample group starting from the notch as evident in the macroexaminations. The fatigue fracture surface morphologies after precrack regions were investigated under SEM. Crystallographic and ductile crack propagation regions were highlighted by red and blue boxes, respectively, in Figure 3.42, Figure 3.43, Figure 3.45 and Figure 3.46.

Figure 3.42 shows the fracture surface features at low and high ΔK of the P20_T-L specimen. Distinctive features such as flat-facets, slip bands, and tear ridges were observed at low ΔK, corresponding to the stage I region. Slip bands formed by plastic deformation of crystallographically favorable planes, appeared as step-like patterns. Higher magnification images of these slip bands are given in Figure 3.42c. Figure 3.42d shows the fracture surface region where the ductile crack propagation dominates over crystallographic crack propagation, corresponding to stage II. Clear fatigue striations were apparent between the tear ridges in this region as shown in Figure 3.42e. Also, this region appeared to be smoother than the fracture surface corresponding to the stage I.

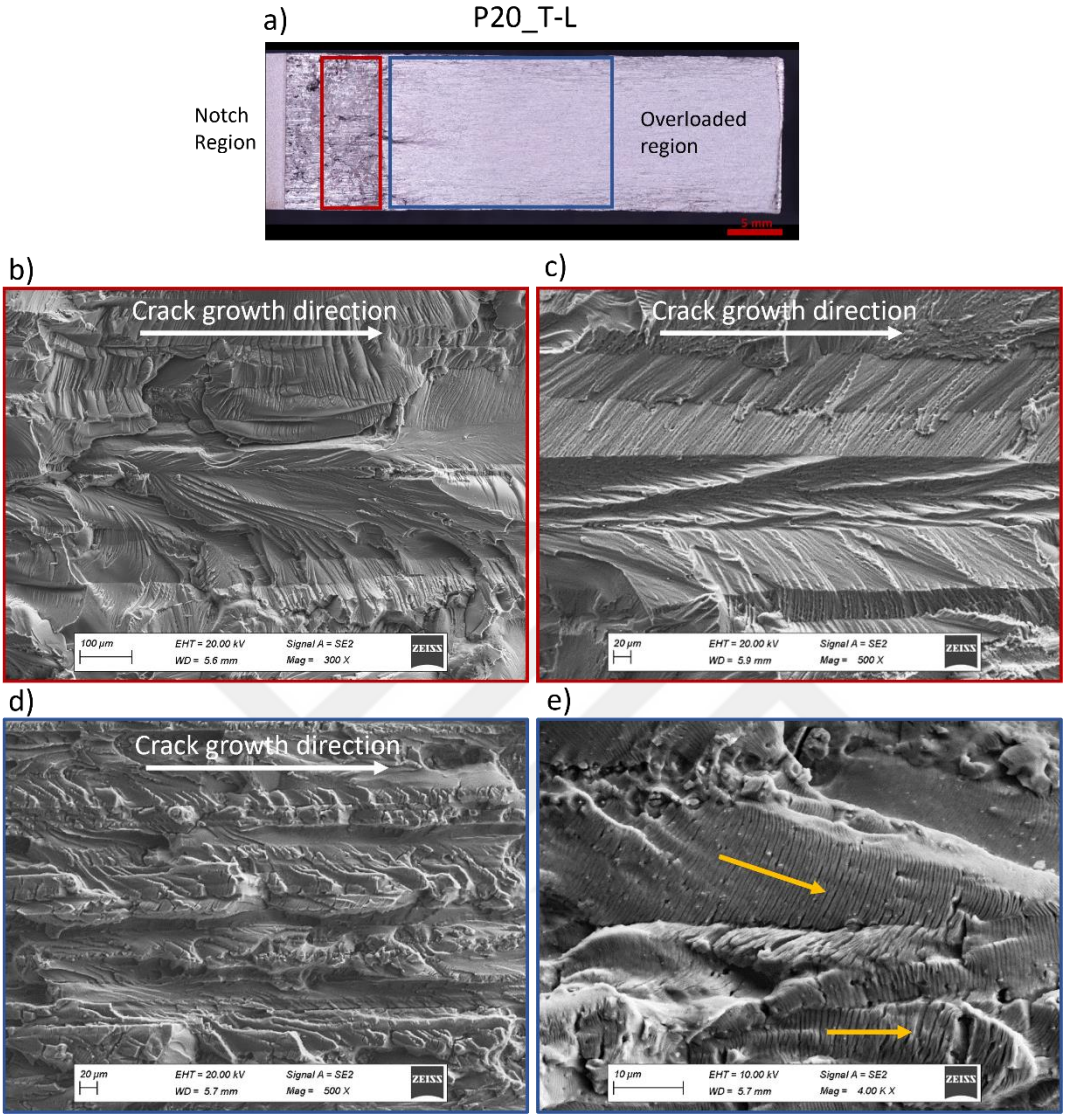

Figure 3.42. a) Stereomicroscope image of the fracture surface and SEM images of (b-c) crystallographic (low ΔK) and (d-e) stable crack growth region (intermediated ΔK) of P20_T-L specimen.

SEM images of fracture surface of P20_L-T are shown in Figure 3.43. In this sample, the facets and slip bands were apparent in both low and intermediate ΔK, as shown in Figure 3.43b and Figure 3.43c. These observations suggested that the crack followed the crystallographic orientation at the intermediate ΔK. Also, fatigue striations were observed at the region indicated by the blue rectangle in Figure 3.43e.

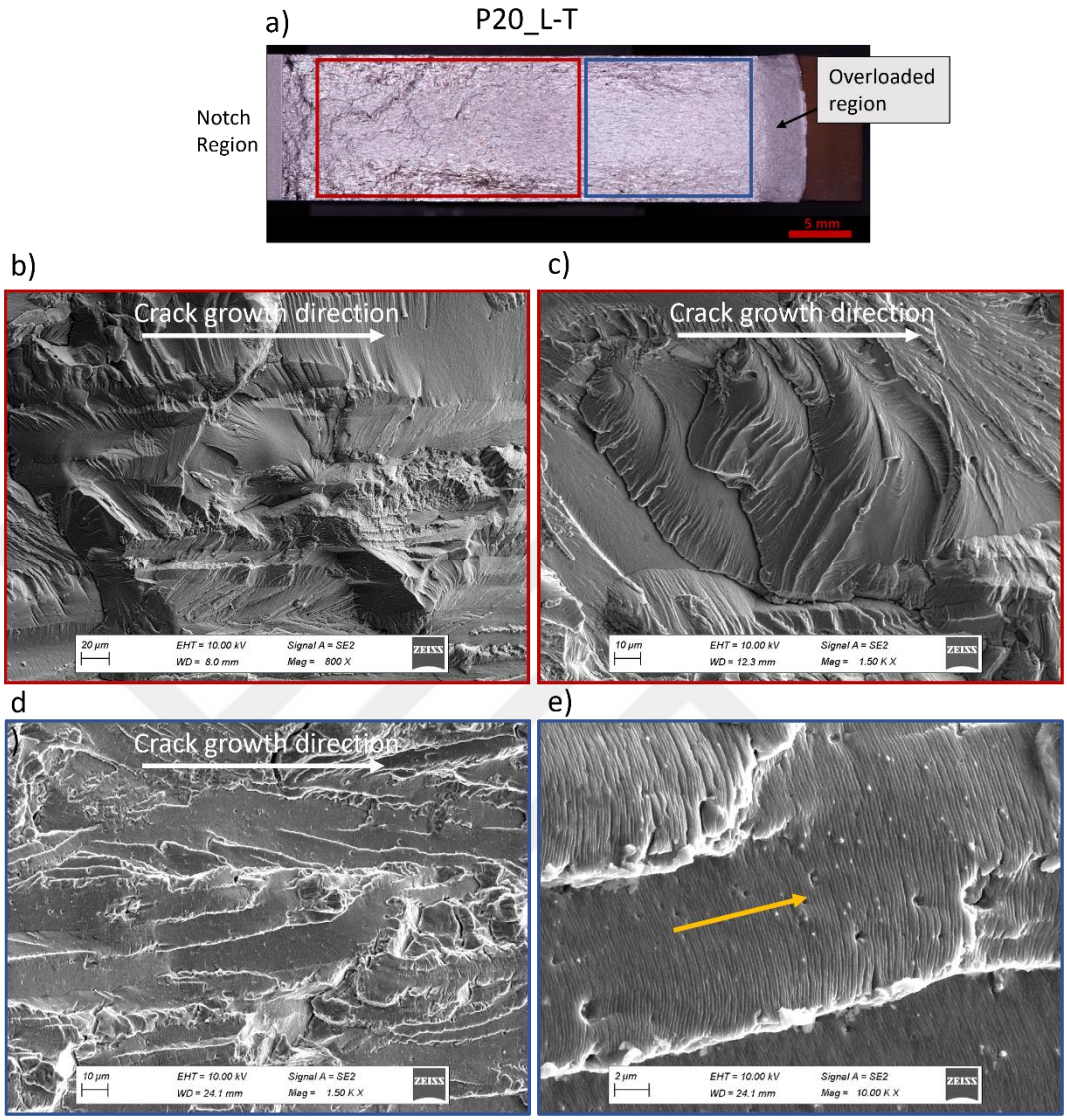

Figure 3.43. a) Stereomicroscope image of the fracture surface and SEM images of (b-c) crystallographic (low and intermediated ΔK) and (d-e) stable crack growth region (high ΔK) of P20_L-T specimen.

The near-crack deviation region of the P20_L-T specimen was also investigated under SEM. Figure 3.44 shows the presence of secondary cracks perpendicular to the crack growth direction. It is important to note that some of these secondary cracks followed the grain boundary regions.

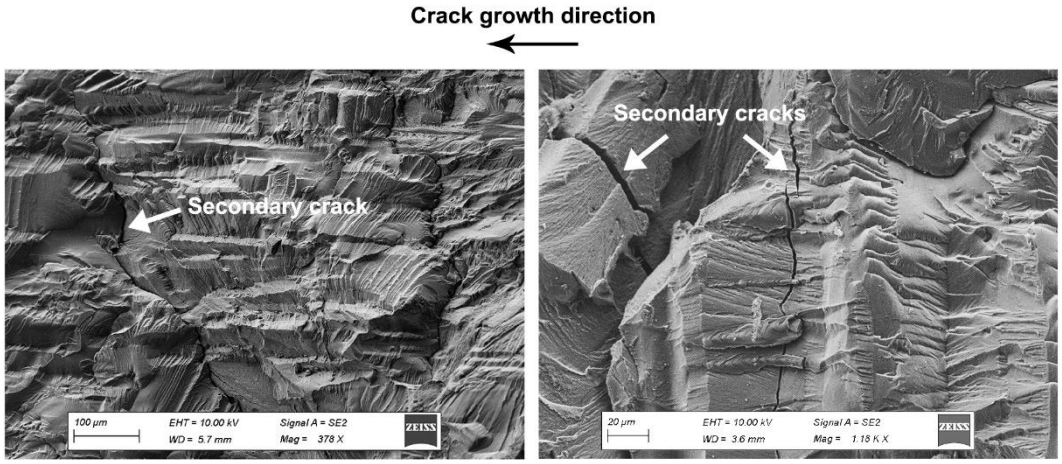

Figure 3.44. SEM images of microcracks perpendicular to the crack growth direction captured from the near-crack region of P20_L-T's fracture surface.

SEM images showing the crack propagation regions of the P130_T-L and P130_L-T specimens are presented in Figure 3.45 and Figure 3.46, respectively. Flat-facets, slip bands and tear ridges were observed in the stage I region (indicated by red frames) of both P130_T-L and P130_L-T samples. Higher magnification images of the slip bands are given in Figure 3.45c and Figure 3.46c for P130_T-L and P130_L-T respectively.

Figure 3.45d and Figure 3.46d display the morphology of the steady-state crack growth zone (stage II) for P130_T-L and P130_L-T samples, respectively. Formation of ductile striations were apparent on the fracture surfaces of both samples. Also, fatigue striations were observed towards the end of the stage I in both samples. SEM images of fatigue striations captured corresponding to the similar ΔK (low and high ΔK regions) are given in Figure 3.45e and Figure 3.46f, for P130_T-L and P130_L-T, respectively. The fatigue striations detected in the P130_L-T sample were relatively finer compared to those observed in the P130_T-L sample. These observations align with the da/dN curves.

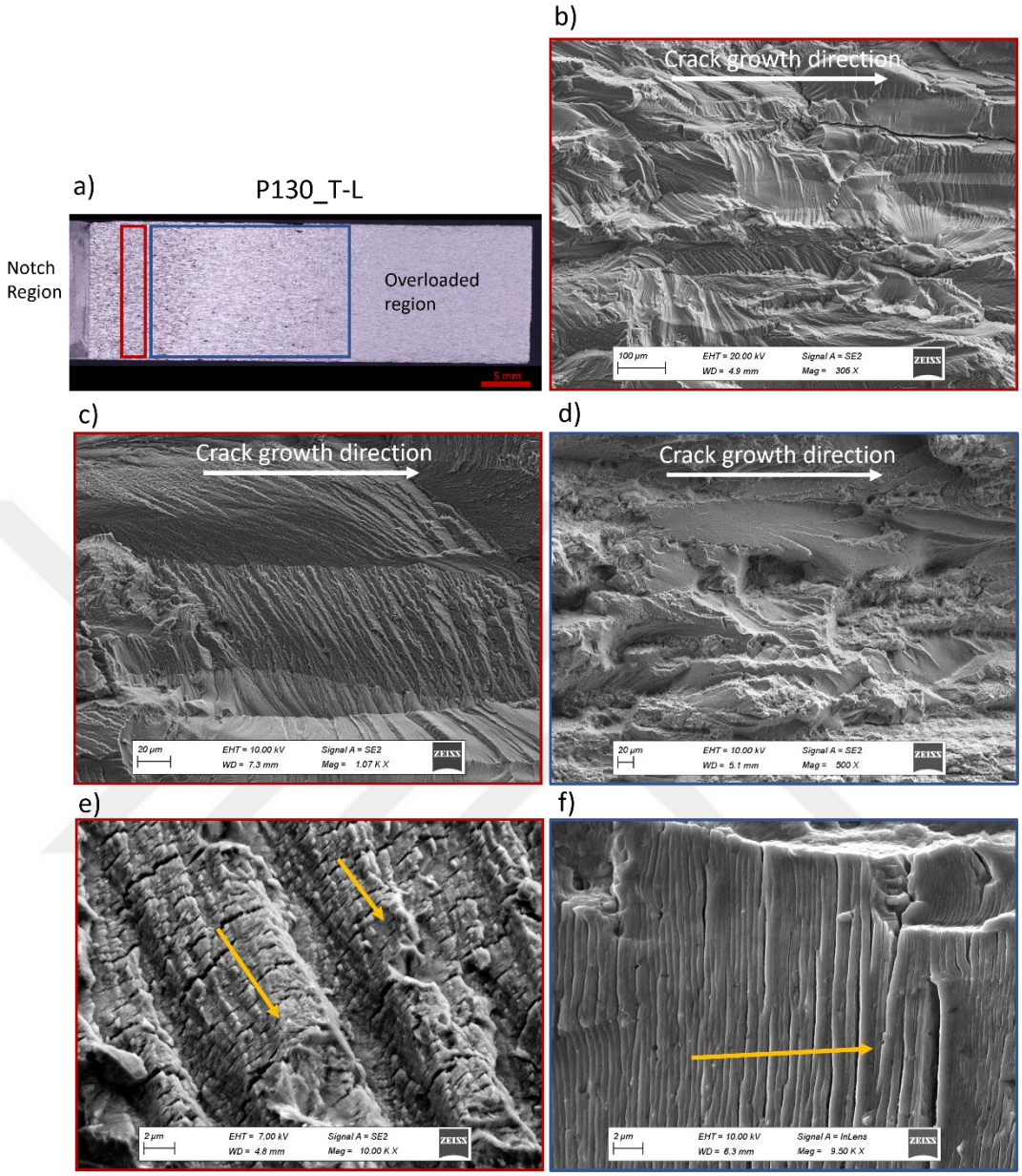

Figure 3.45. a) Stereomicroscope image of the fracture surface and SEM images of (b-c) crystallographic (low ΔK), d) stable crack growth region (intermediated ΔK) (f-e) fatigue striations at intermediated and high ΔK in P130_T-L specimen.

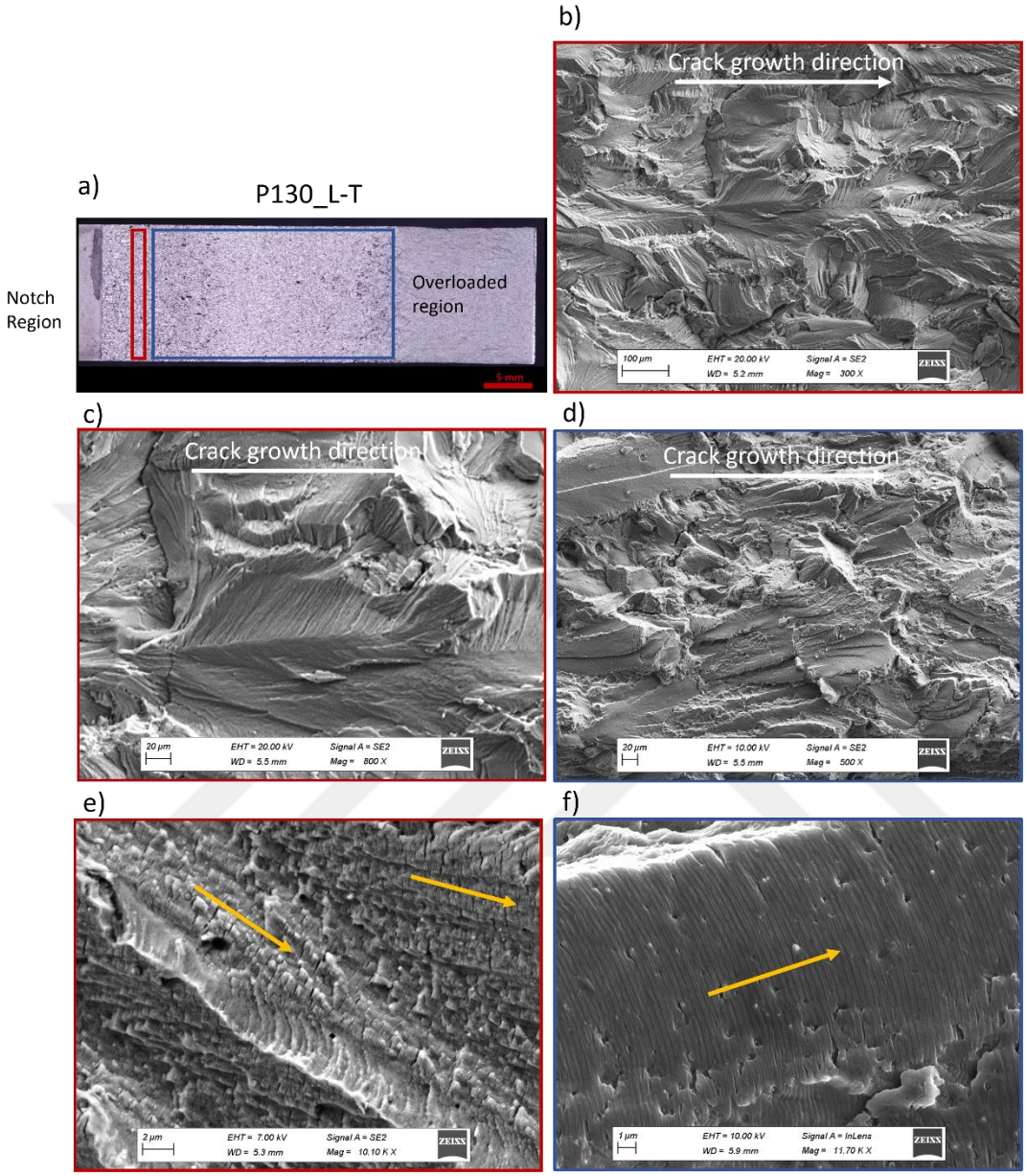

Figure 3.46. a) Stereomicroscope image of the fracture surface and SEM images of (b-c) crystallographic (low ΔK), d) stable crack growth region (intermediated ΔK) (f-e) fatigue striations at intermediated and high ΔK in P130_L-T specimen.

SEM images of the fast fracture zone for each specimen were given in Figure 3.47. Dimpled structure, indicating a ductile fracture, was observed in the fast fracture region of the samples.

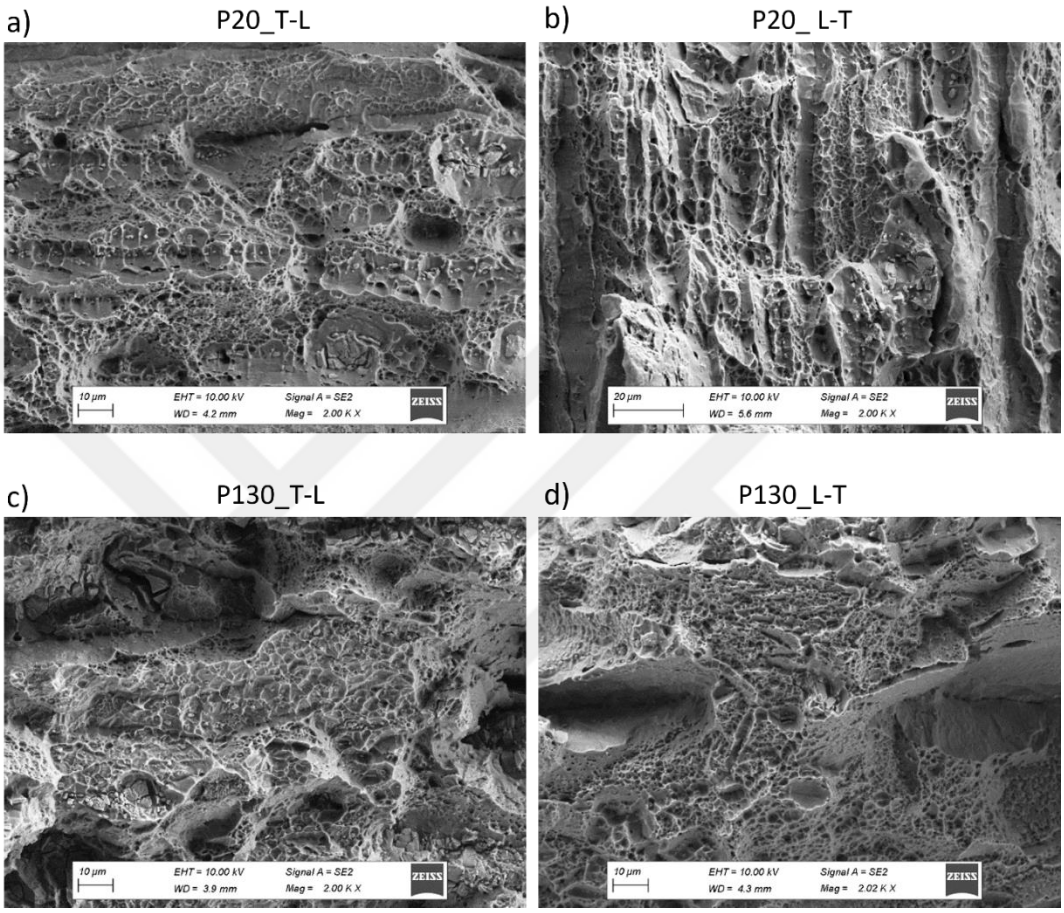

Figure 3.47. SEM images of the fast fracture zone of a) P20_T-L, b) P20_L-T, c) P130_T-L, and d) P130_L-T.

Fatigue striation spacing around the second phase particles was observed to be decreased as shown in Figure 3.48. This observation was an indication of reduced crack propagation rate due to the second phase particles. The effect of second phase particles on the crack growth rate was not expected to cause any significant difference between the sample groups, as all the sample groups had similar amount of second phase particles.

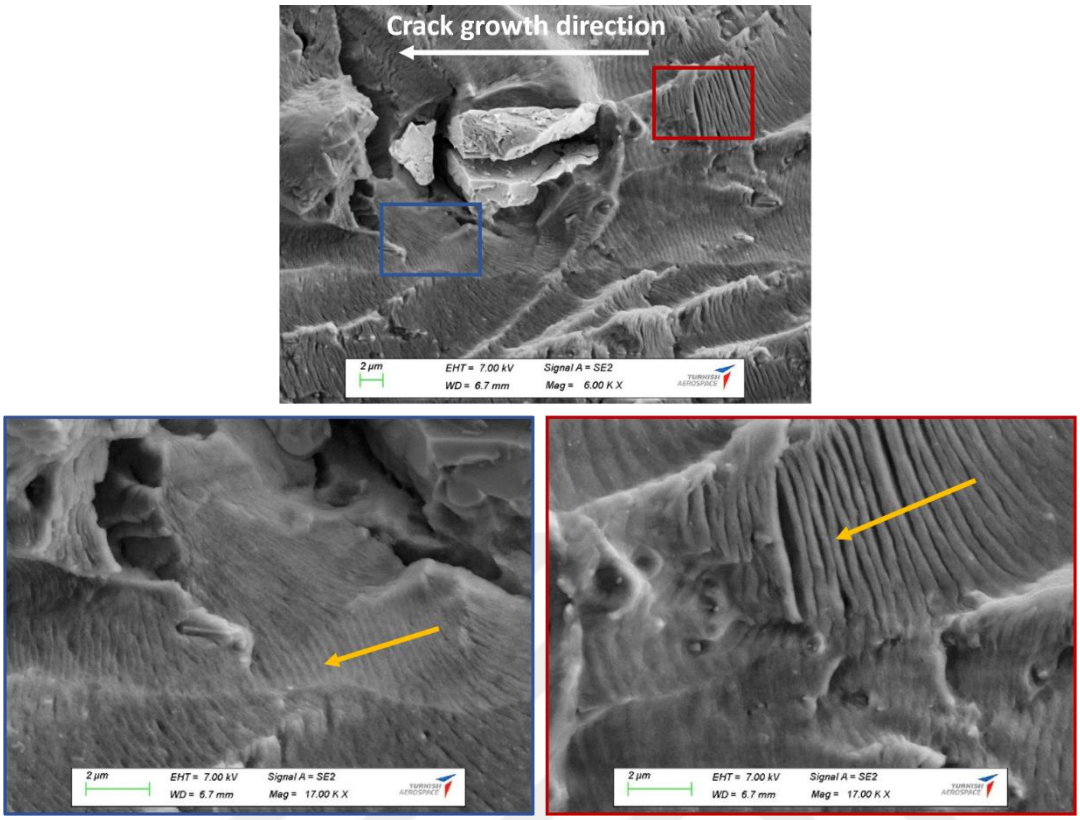

Figure 3.48. SEM images of the fatigue striations around the second phase particles.

There was a significant crack path deviation in the fatigue crack growth tests of the P20_L-T sample. To better understand the reason of the crack deviation, individual and collective effects of all proposed mechanisms in the literature should be considered. These mechanisms in aluminum alloys included the amount of recrystallization, grain boundary strength (which is related to grain misorientation), texture, orientation of the specimen, and tendency of slip band formation [37]. It should also be noted that it is highly difficult to estimate the individual effect of these parameters on crack propagation. Still, the effect of the recrystallization state can be assumed not to cause any difference in the crack propagation in our samples, as all the samples are in an unrecrystallized state [38]. No significant effect of slip band formation tendency on the crack deviation in the P20_L-T was also expected. Slip band formation is favorable in AA2050 alloys due to having shearable T1 precipitates as the main hardening phase [39], and slip bands appeared on the fracture

surfaces of all samples at low ΔK. Therefore, the crack deviation in P20_L-T was mainly attributed to two reasons. First, the load is applied to the P20_L-T sample in the rolling direction. Therefore, the initial crack propagation direction is perpendicular to the highly elongated grains. Esin et al. [25] showed that a 100 mm thick AA2050-T84 plate had a similar crack path deviation in this loading condition. They proposed a possible mechanism for this crack deviation which included the formation of microcracks parallel to the loading direction, which was also observed in the P20_L-T sample (see Figure 3.44) in this study. Those microcracks were observed to follow grain boundary regions which could be attributed to the weakened grain boundaries due to the formation of precipitation-free zones [40].

The second reason for the crack deviation in P20_L-T might be the texture formation in the LT-ST plane. The preferred orientation of the grains along (200) planes are apparent in the normalized XRD pattern of the LT-ST plane of the 20 mm-thick plates (see Figure 3.12). This finding was confirmed by EBSD analysis. The variation of crystal orientation of the LT-ST planes of the specimens extracted from 20 mm and 130 mm plates was characterized using EBDS. The LT-ST plane is the plane where crack propagation occurs in L-T orientated samples (Figure 4.47a). The reason for choosing this plane for EBSD analysis was that crack path deviation is observed in the P20_L-T specimens. A sketch is given in Figure 3.49a showing the orientation of the CT specimen for P20_L-T and the LT-ST plane, of which the EBSD analysis was carried out. EBSD analysis was also done on the LT-ST plane of the 130 mm thick plate for comparison. The orientation maps of LT-ST planes of 20- and 130-mm thick plates are shown in Figure 3.49b and Figure 3.49c, respectively. The inverse pole graphs were also shown in Figure 3.49d and Figure 3.49e, for the LT-ST planes of 20 mm and 130 mm thick plates, respectively. It is evident in both EBSD micrographs and inverse pole figures that there is a texture evolution in 20 mm thick plate, whereas no preferential orientation was observed for 130 mm thick plate. This finding was in agreement with the XRD patterns of the samples obtained from their LT-ST planes. These findings indicated that the misorientation angles between the adjacent grains in the LT-ST plane of 20 mm thick

sample are small. Therefore, easy propagation of slip band can be expected across several grains, forming a preferential crack path [37]. The optical microscope image shown in Figure 3.50 of the L-T sample aligns with this observed behavior. Also, the crack was expected to follow (111) plane due to its low surface energy and ease of dislocation motion than the other planes, such as (200). These factors were thought to contribute the crack path deviation in P20_L-T sample.

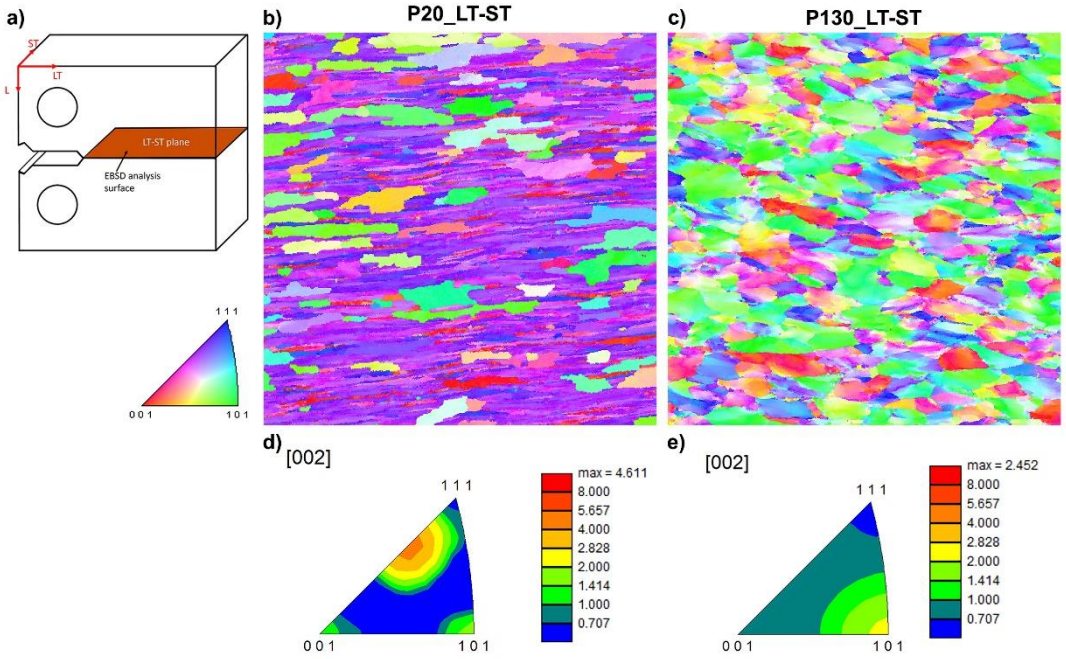

Figure 3.49. a) Schematic drawing showing the position of LT-ST plane in the L-T oriented FCG test specimen and the orientation maps obtained from the LT-ST planes of b) 20 and c) 130 mm thick plate and inverse pole figures obtained from the LT-ST planes of d) 20 and e) 130 mm thick plate

Figure 3.50. Optical microscope image of the deviated crack in P20_L-T sample.

CHAPTER 4

CONCLUSIONS

In this study, the effect of microstructural alterations including grain anisotropy (aspect ratio), elongation and orientation on the mechanical properties of AA2050-T84 alloy was characterized. The main conclusions of the study can be summarized as follows:

- AA2050-T84 plates have anisotropic microstructures with elongated grains in the rolling direction. While the maximum aspect ratio was measured as 9 for 130 mm thick plate on the L-ST plane, it was measured as 27 on the L-ST plane of 20 mm thick plate. This result was attributed to the higher extent of rolling applied to the 20 mm thick plate.
- An evident crystallographic orientation was observed in 20 mm thick plate on the LT-ST plane showing a preference towards (200) and (220) planes indicating a texture evolution.
- 20 mm thick plate had slightly higher tensile and yield strength than the 130 mm thick plate in both L and LT directions. Also, yield strengths of both plates were slightly higher in the L direction compared to the LT direction.
- 20 mm thick plate had slightly lower FCGR than 130 mm thick plate when the loading direction was perpendicular to the rolling direction. The fractographic analysis of these plates under this loading condition exhibited crystallographic crack path (apparent slip bands on the fracture surface) at low ΔK and a more ductile fracture path (formation of striations) at intermediate and high ΔK.
- A significant crack deviation ($> 20^{o}$) was observed in the FCG tests of 20 mm thick plate when loading direction was parallel to the rolling direction.
- Two possible reasons were proposed to explain the crack deviation observed in 20 mm thick plate. First, microcracks along grain boundaries

(perpendicular to the initial crack propagation direction) were apparent at the near crack deviation region on the fracture surface of the samples and may cause crack deviation. The second reason may be the presence of a texture on the expected crack plane (LT-ST). The presence of the texture caused a small misorientation between adjacent grains, causing easy propagation of slip bands across several grains. Also, the crack was expected to follow (111) plane due to its low surface energy and ease of dislocation motion than the other planes, such as (200), forming a preferential crack path.

The results obtained in this study are anticipated to make a valuable contribution to the existing knowledge about the AA2050 alloy, particularly in the context of its application in the aerospace industry.

REFERENCES

[1] Pickens, J. R. (1985). The weldability of lithium-containing aluminum alloys. Journal of materials science, 20, 4247-4258.

[2] Pickens, J. R. (1990). Recent developments in the weldability of lithium-containing aluminum alloys. Journal of Materials Science, 25, 3035-3047.

[3] Ivanov, R., Boselli, J., Denzer, D., Larouche, D., Gauvin, R., & Brochu, M. (2016). Hardening Potential of an Al-Cu-Li Friction Stir Weld. In ICAA13 Pittsburgh: Proceedings of the 13th International Conference on Aluminum Alloys (pp. 659-664). Springer International Publishing.

[4] Rioja, R. J., & Liu, J. (2012). The evolution of Al-Li base products for aerospace and space applications. Metallurgical and Materials Transactions A, 43(9), 3325-3337.

[5] Starke, E. A., & Lin, F. S. (1982). The influence of grain structure on the ductility of the Al-Cu-Li-Mn-Cd alloy 2020. Metallurgical Transactions A, 13, 2259-2269.

[6] Starke, E. A., Sanders, T. H., & Palmer, I. G. (1981). New approaches to alloy development in the Al-Li system. JOM, 33, 24-33.

[7] Quist, W. E., Narayanan, G. H., & Wingert, A. L. (1983). Aluminum-lithium alloys for aircraft structure- An overview. Aluminum-lithium alloys II, 313-334.

[8] Starke Jr, E. A., & Staley, J. T. (1996). Application of modern aluminum alloys to aircraft. Progress in aerospace sciences, 32(2-3), 131-172.

[9] Lavernia, E. J., Srivatsan, T. S., & Mohamed, F. A. (1990). Strength, deformation, fracture behaviour and ductility of aluminium-lithium alloys. Journal of Materials Science, 25, 1137-1158.

[10] Starke Jr, E. A. (2014). Historical development and present status of aluminum–lithium alloys. In Aluminum-lithium alloys (pp. 3-26). Butterworth-Heinemann.

[11] Miller, W. S., Zhuang, L., Bottema, J., Wittebrood, A., De Smet, P., Haszler, A., & Vieregge, A. J. M. S. (2000). Recent development in aluminium alloys for the automotive industry. Materials Science and Engineering: A, 280(1), 37-49.

[12] Rioja, R. J. (1998). Fabrication methods to manufacture isotropic Al-Li alloys and products for space and aerospace applications. Materials Science and Engineering: A, 257(1), 100-107.

[13] Jata, K. V., Panchanadeeswaran, S., & Vasudevan, A. K. (1998). Evolution of texture, micro structure and mechanical property anisotropy in an Al-Li-Cu alloy. Materials Science and Engineering: A, 257(1), 37-46.

[14] Sanders Jr, T. H., & Starke Jr, E. A. (1982). The effect of slip distribution on the monotonic and cyclic ductility of Al□ Li binary alloys. Acta Metallurgica, 30(5), 927-939.

[15] Cassada, W. A., Shiflet, G. J., & Starke Jr, E. A. (1986). The effect of germanium on the precipitation and deformation behavior of Al2Li alloys. Acta metallurgica, 34(3), 367-378.

[16] Prasad, N. E., Gokhale, A., & Wanhill, R. J. (Eds.). (2013). Aluminum-lithium alloys: processing, properties, and applications. Butterworth-Heinemann.

[17] Dursun, T., & Soutis, C. (2014). Recent developments in advanced aircraft aluminium alloys. Materials & Design (1980-2015), 56, 862-871.

[18] Polmear, I. J. (1986). Development of an Experimental Wrought Aluminium Alloy for Use at Elevated Temperatures. Aluminum Alloys–Their Physical and Mechanical Properties, 1, 661-674.

[19] Bodily, B., Heinimann, M., Bray, G., Colvin, E., & Witters, J. (2012). Advanced aluminum and aluminum-lithium solutions for derivative and next generation aerospace structures (No. 2012-01-1874). SAE Technical Paper.

[20] Lequeu, P., Smith, K. P., & Daniélou, A. (2010). Aluminum-copper-lithium alloy 2050 developed for medium to thick plate. Journal of materials engineering and performance, 19, 841-847.

[21] Niedzinski, M. (2019). The evolution of constellium Al-Li alloys for space launch and crew module applications. Light Metal Age, 77, 36-42.

[22] Cassada, W. A., Shiflet, G. J., & Starke, E. A. (1991). The effect of plastic deformation on Al 2 CuLi (T 1) precipitation. Metallurgical Transactions A, 22, 299-306.

[23] Kulkarni, G. J., Banerjee, D., & Ramachandran, T. R. (1989). Physical metallurgy of aluminum-lithium alloys. Bulletin of Materials Science, 12, 325-340.

[24] Hafley, R. A., Domack, M. S., Hales, S. J., & Shenoy, R. N. (2011). Evaluation of Aluminum Alloy 2050-T84 Microstructure and Mechanical Properties at Ambient and Cryogenic Temperatures (No. NF1676L-24863).

[25] Esin, V. A., François, M., Belkacemi, L. T., Irmer, D., Briez, L., & Proudhon, H. (2022). Effect of microstructure on fatigue crack deviation in AA2050-T84. Materials Science and Engineering: A, 858, 144120.

[26] Nizery, E., Proudhon, H., Buffiere, J. Y., Cloetens, P., Morgeneyer, T. F., & Forest, S. (2015). Three-dimensional characterization of fatigue-relevant intermetallic particles in high-strength aluminium alloys using synchrotron X-ray nanotomography. Philosophical Magazine, 95(25), 2731-2746.

[27] Lu, D. D., Li, J. F., Hong, N. I. N. G., CHEN, Y. L., ZHANG, X. H., Zhang, K., ... & ZHANG, R. F. (2021). Effects of microstructure on tensile properties of AA2050-T84 Al-Li alloy. Transactions of Nonferrous Metals Society of China, 31(5), 1189-1204.

[28] Anderson, T. L. (2017). Fracture mechanics: fundamentals and applications. 4th Ed. CRC press.

[29] Cavalcante, T. R. F., Pereira, G. S., Koga, G. Y., Bolfarini, C., Bose Filho, W. W., & Avila, J. A. (2022). Fatigue crack propagation of aeronautic AA7050-T7451 and AA2050-T84 aluminum alloys in air and saline environments. International Journal of Fatigue, 154, 106519.

[30] Ranganathan, N., Adiwijayanto, F., Petit, J., & Bailon, J. P. (1995). Fatigue crack propagation mechanisms in an aluminium lithium alloy. Acta metallurgica et materialia, 43(3), 1029-1035.

[31] Dorin, T., Vahid, A., & Lamb, J. (2018). Aluminium Lithium Alloys. In: Fundamentals of Aluminium Metallurgy, 387–438.

[32] Csontos, A. A., & Starke, E. A. (2005). The effect of inhomogeneous plastic deformation on the ductility and fracture behavior of age hardenable aluminum alloys. International Journal of Plasticity, 21(6), 1097-1118.

[33] Schubbe, J. J. (2009). Fatigue crack propagation in 7050-T7451 plate alloy. Engineering Fracture Mechanics, 76(8), 1037-1048.

[34] Aghamohammadi, H., Hosseinipour, S. J., Rabiee, S. M., & Jamaati, R. (2021). Effect of hot rolling on microstructure, crystallographic texture, and hardness of AZ31 alloy. Materials Chemistry and Physics, 273, 125130.

[35] Ludtka, G. M., & Laughlin, D. E. (1982). The influence of microstructure and strength on the fracture mode and toughness of 7XXX series aluminum alloys. Metallurgical Transactions A, 13, 411-425.

[36] Bucci, R. J. (1979). Selecting aluminum alloys to resist failure by fracture mechanisms. Engineering Fracture Mechanics, 12(3), 407-441.

[37] Kamp, N., Gao, N., Starink, M. J., & Sinclair, I. (2007). Influence of grain structure and slip planarity on fatigue crack growth in low alloying artificially aged 2xxx aluminium alloys. International journal of fatigue, 29(5), 869-878.

[38] Abd El-Aty, A., Xu, Y., Guo, X., Zhang, S. H., Ma, Y., & Chen, D. (2018). Strengthening mechanisms, deformation behavior, and anisotropic mechanical properties of Al-Li alloys: A review. Journal of advanced research, 10, 49-67.

[39] Guérin, M., Alexis, J., Andrieu, E., Blanc, C., & Odemer, G. (2015). Corrosion-fatigue lifetime of Aluminium–Copper–Lithium alloy 2050 in chloride solution. Materials & Design, 87, 681-692.

[40] Morgeneyer, T. F., Starink, M. J., Wang, S. C., & Sinclair, I. (2008). Quench sensitivity of toughness in an Al alloy: Direct observation and analysis of failure initiation at the precipitate-free zone. Acta Materialia, 56(12), 2872-2884.